

# The internal rotation profile of the B-type star KIC 10526294 from frequency inversion of its dipole gravity modes and statistical model comparison

S. A. Triana, E. Moravveji<sup>1</sup>, P. I. Pápics<sup>2</sup>,

*Institute of Astronomy, KU Leuven, Celestijnenlaan 200D, Leuven, Belgium*

C. Aerts,

*Institute of Astronomy, KU Leuven, Celestijnenlaan 200D, Leuven, Belgium*

*Department of Astrophysics/IMAPP, Radboud University Nijmegen, 6500 GL Nijmegen,  
The Netherlands*

S. D. Kawaler,

*Department of Physics and Astronomy, Iowa State University, Ames, IA 50011, USA*

and

J. Christensen-Dalsgaard

*Stellar Astrophysics Centre, Department of Physics and Astronomy, Aarhus University,  
DK8000 Aarhus C, Denmark*

## ABSTRACT

The internal angular momentum distribution of a star is key to determine its evolution. Fortunately, the stellar internal rotation can be probed through studies of rotationally-split nonradial oscillation modes. In particular, detection of nonradial gravity modes (g modes) in massive young stars has become feasible recently thanks to the *Kepler* space mission. Our aim is to derive the internal rotation profile of the *Kepler* B8V star KIC 10526294 through asteroseismology. We interpret the observed rotational splittings of its dipole g modes using four different approaches based on the best seismic models of the star and their rotational kernels. We show that these kernels can resolve differential rotation within

---

<sup>1</sup>Postdoctoral Fellow of the Federal Science Policy Office of Belgium (Belspo)

<sup>2</sup>Postdoctoral Fellow of the Fund for Scientific Research of Flanders (FWO), Belgium

the radiative envelope if a smooth rotational profile is assumed and the observational errors are small. Based on *Kepler* data, we find that the rotation rate near the core-envelope boundary is well constrained to  $163 \pm 89$  nHz. The seismic data are consistent with rigid rotation but a profile with counter-rotation within the envelope has a statistical advantage over constant rotation. Our study should be repeated for other massive stars with a variety of stellar parameters in order to deduce the physical conditions that determine the internal rotation profile of young massive stars, with the aim to improve the input physics of their models.

*Subject headings:* Asteroseismology – Stars: rotation – Stars: oscillations (including pulsations) – Stars: individual: KIC 10526294

## 1. Introduction

One of the major important ingredients in the computation of stellar evolution models, from the star formation process until the death of the star, is rotation (e.g., Maeder 2009, for a recent monograph in the subject). Even in the case of slow rotation, the dynamical and mixing processes related to it are not negligible as they substantially affect the structure of the star. Unfortunately, direct measurements of the internal rotation profile of stars are not possible. Hence the inclusion of rotational effects in models rests on uncalibrated theoretical prescriptions.

It is a fortunate circumstance that the oscillation frequencies of a star are affected by its rotational properties (Ledoux 1951). The frequency splitting of the oscillation modes is well understood in the case of slowly rotating stars for which a first-order perturbation method is sufficient to model the frequencies (e.g. Aerts et al. 2010, for an extensive description). In this work, we assume that we are dealing with an unevolved star that does not possess a magnetic field and whose central frequencies of the rotationally-split multiplets are not affected by the slow rotation. Moreover, we assume that the deformation from spherical symmetry due to the centrifugal forces can be ignored. In that case the frequency splitting of the oscillation modes, as measured in the observer’s frame, is due to a combination of mode advection and the Coriolis force and can be computed from the so-called rotational kernels (cf. Eq.(3.356) in Aerts et al. 2010).

Helioseismology delivered a very detailed view of the internal rotation profile  $\Omega(r, \theta)$  of the Sun for the radial range  $r \in [0.2 R_\odot, 1.0 R_\odot]$  ( $R_\odot$  denotes the solar radius) and for all co-latitudes  $\theta$ , through frequency inversion of the rotational splittings of its hundreds of detected acoustic modes (e.g., Christensen-Dalsgaard 2002; Thompson et al. 2003), a technique that

has found its way even to laboratory experiments (Triana et al. 2014). Given that acoustic modes do not have sufficient probing power in the very inner regions and that the Sun does not reveal gravity modes, it is not possible to deduce the rotational profile for  $r \lesssim 0.2 R_{\odot}$ .

It is not currently within reach to derive the rotation profile for distant stars with similar precision as the Sun, but applications of asteroseismology did allow to deduce averaged rotation rate ratios  $\Omega_{\text{core}}/\Omega_{\text{envelope}}$  from forward modeling of the rotational splitting for a few main-sequence B stars from ground-based monitoring campaigns (Aerts et al. 2003; Pamyatnykh et al. 2004; Briquet et al. 2007), as well as two  $\delta$  Sct- $\gamma$  Dor-type hybrid main-sequence pulsators from *Kepler* space-based photometry (Kurtz et al. 2014; Saio et al. 2015). Moreover,  $\Omega_{\text{core}}$  was derived from gravity-dominated mixed modes in hundreds of red giants observed with *Kepler* (Beck et al. 2012; Mosser et al. 2012), while the estimate of their  $\Omega_{\text{envelope}}$  is uncertain due to the remaining dominant influence of the core regions on the measured splittings of the pressure-dominated mixed modes. Deheuvels et al. (2012) and Deheuvels et al. (2014) performed frequency inversions for seven selected subgiants in different evolutionary stages relying on the splitting of their dipole mixed modes. They selected profiles representing a linear decrease in rotation frequency in the core regions followed by a constant rotation profile in the extended convective envelope, with  $\Omega_{\text{core}}/\Omega_{\text{envelope}}$  ranging from 2 to about 20. A similar result was obtained for the red giant KIC 5006817, which is the primary of an eccentric binary, by Beck et al. (2014). Only in some of those studies, e.g. Deheuvels et al. (2014), statistical model comparison was used to evaluate the likelihood of the optimal shape of the rotational frequency throughout the stars and few continuous and discontinuous functions for  $\Omega(r)$  were considered. Despite their frequent occurrence in e.g., geophysics, counter-rotating solutions were considered inappropriate for stars. Independently of that restriction, the *Kepler* results for  $\Omega(r)$  so far deliver an important calibration for the improvement of evolutionary models for single and binary low-mass stars, given that the theoretical predictions of angular-momentum transport result in core rotation rates are higher by at least an order of magnitude than observed (see e.g. Eggenberger et al. 2012; van Saders & Pinsonneault 2013; Cantiello et al. 2014, for the input physics in question). The need for redistribution and loss of angular momentum during evolution is also required on the basis of the internal rotation properties of white dwarfs derived from both forward modeling and inversion of their rotationally-split g mode oscillation frequencies (Charpinet et al. 2009; Córscico et al. 2012).

In this work, we provide the first frequency inverted rotation profile of an unevolved intermediate-mass B-type main-sequence star from its rotationally-split dipole gravity modes detected in four years of *Kepler* data. The paper is organized as follows: we summarize the observational data and the results of forward seismic modeling in Section 2. In Sections 3 and 4 we examine in detail the rotational kernels and the splittings associated with linear

rotation models. In Section 5 we present piece-wise two- and three-zone rotation models. Section 6 is devoted to inversion methods, including theory and results, and in Section 7 we present results for the rotation profile based on Monte Carlo simulations. We summarize and conclude in Section 8.

## 2. Observational input and results of forward seismic modeling

A first detailed asteroseismic analysis of the main sequence B star KIC 10526294, was presented by Pápics et al. (2014), including an estimation of the amount of core overshooting following earlier approaches for main-sequence B stars with a well-developed convective core. They characterized KIC 10526294 as a slowly rotating SPB star (see e.g. Aerts et al. (2010) for a definition) exhibiting a series of 19 quasi-equally spaced dipole modes. KIC 10526294 is so far the only multiperiodic SPB star with unambiguous detection of rotationally-split triplets from the *Kepler* light curve. For this reason, it allows us to probe its interior structure to a deeper level than for any other SPB so far.

With the purpose of detailed seismic modeling, Moravveji et al. (2015) elaborated on optimal frequency error estimation, taking into account the signal-to-noise ratio, sampling, and correlated nature of the *Kepler* data, following the method by Degroote et al. (2009). This resulted in a correction factor of 3.0 to be applied to the formal errors obtained from the nonlinear least-squares fit. We estimated the splitting for each dipole mode as the average splitting between the measured  $m = +1$  and  $m = -1$  peaks with respect to the central  $m = 0$  peak. This comes down to considering only the symmetric component of the splittings. The total variance was then estimated as the variance of the symmetric component plus the *inter*-variance:

$$\sigma_{\text{Total}}^2 = \frac{1}{2} (\sigma_{-1}^2 + \sigma_{+1}^2) + \sigma^2(\delta_{-1}, \delta_{+1}), \quad (1)$$

where  $\delta_{\pm 1}$  denotes the  $m = \pm 1$  splittings and  $\sigma_{\pm 1}$  their individual uncertainties. This results in larger errors for those splittings with larger asymmetric components. Further, as explained by the authors, the error estimates for the triplet components as computed from the Rayleigh limit and taking into account mode crowding effects are too large (Pápics et al. 2014, their Fig. 8). Nevertheless, we also used those overestimated values with the argument that they deliver the most conservative upper limit to the true frequency errors. We list both error sets in Table 1 and show in this work that our conclusions on  $\Omega(r)$  are essentially independent on the choice of error set. The best error estimates (Error Set 1) are used throughout the main text, while all results relying on the too large errors (Error Set 2) are treated in Appendix A.

Following an essentially identical approach as in Pápics et al. (2014), Moravveji et al. (2015) were able to find seismic models that match more closely the observed frequencies

Table 1. Symmetric components of the observed rotational splittings of KIC 10526294

Central frequency [ $\mu\text{Hz}$ ]	Splitting $\delta_{nlm}$ [nHz]	Error Set 1 [nHz]	Error Set 2 [nHz]
5.4655	45.28	14.72	16.54
5.6272	29.49	0.69	8.70
5.7978	33.91	7.37	8.81
5.9873	32.64	7.47	10.33
6.1739	41.99	4.42	7.56
6.3959	35.74	0.36	4.91
6.6200	29.43	4.06	7.38
6.8703	30.42	0.55	8.55
7.1235	33.07	3.46	6.09
7.4213	29.99	1.00	9.41
7.7616	41.55	15.04	17.17
8.1163	28.73	1.03	6.42
8.5036	29.50	2.59	7.75
8.9398	28.18	3.18	7.23
9.4090	27.53	0.85	4.63
9.9115	26.11	1.67	5.82
10.4495	26.41	7.02	10.04
11.0429	25.74	0.49	5.21
11.7293	23.32	4.55	9.34

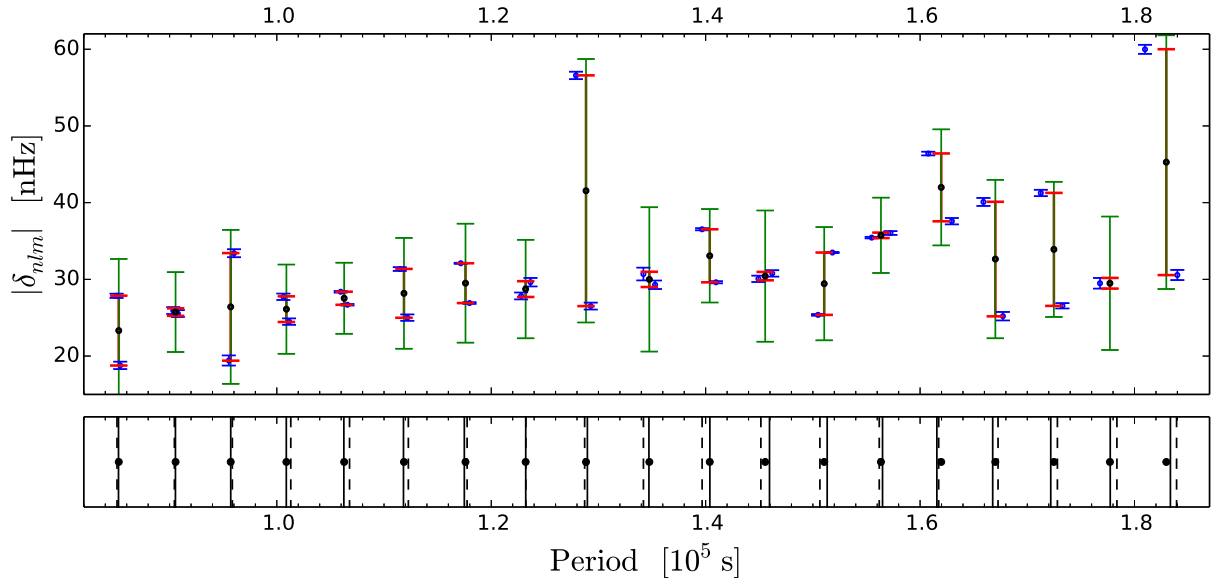


Fig. 1.— Top: Observed rotational splittings (top panel, blue error bars), and the symmetric component used as inversion inputs (top panel, red error bars). The errors on the inversion inputs were taken from Moravveji et al. (2015) and the green error bars are from Pápics et al. (2014), see text for details). We chose the abscissae of the inversion inputs so as to coincide with the central  $m = 0$  peak of the observed triplets. Bottom: the location of the central peaks as black dots, and the mode periods from models: vertical solid lines for the best model in Moravveji et al. (2015) (Model 1), vertical dashed lines for the best model in Pápics et al. (2014) (Model 2).

thanks to the inclusion of extra diffusive mixing in the stellar envelope, in addition to core overshooting. Such additional mixing was already found necessary for the B3V SPB star HD 50230 (Degroote et al. 2010). The parameters of the two models are given in Table 2. We base the present work on the best matching Model 1 from Moravveji et al. (2015) but we checked that the main qualitative features of the resulting rotation profiles from inversion do not depend on the choice of the seismic model, as long as it is able to reproduce reasonably well the main observed characteristics of the star. We return to this in Section 6.3.

In a non-rotating star, oscillation mode families are characterized by their radial order  $n$  and degree  $l$ , with individual family members corresponding to different values of  $m$ , the azimuthal wave number, sharing the same eigenfrequency. Rotation lifts this degeneracy. The identification of the radial order  $n$  of the 19 detected modes of KIC 10526294 was achieved by comparing the periods of the observed zonal ( $m = 0$ ) dipole ( $l = 1$ ) g modes with those predicted by equilibrium models computed with the MESA stellar structure and

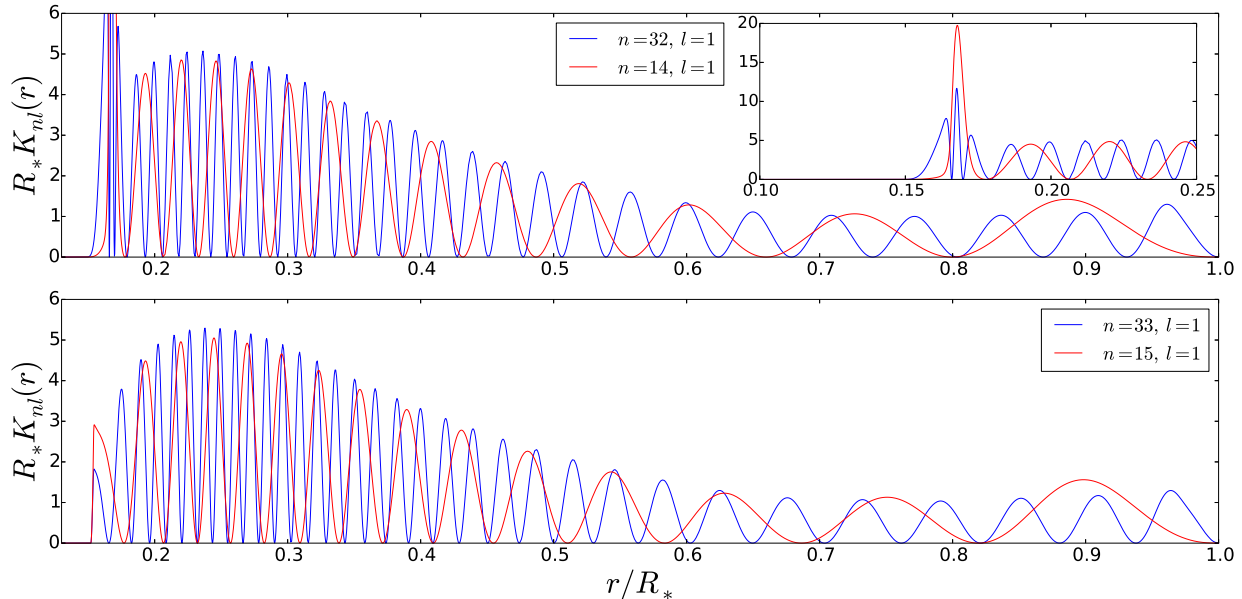


Fig. 2.— The rotational kernels of dipole zonal modes of highest and lowest radial order, plotted against the stellar fractional radius  $r/R_*$ , for the best matching models found by Pápics et al. (2014, lower panel) and Moravveji et al. (2015, upper panel) — cf. lower panel of Fig. 1. Some of the modes in the upper panel are trapped near the convective core as evidenced by the large peak just outside the convective core, as visible in the inset. The kernels from the best seismic model found by Pápics et al. (2014) shown in the bottom panel do not exhibit trapping, but the overall shapes are similar otherwise. Inversion results from both of these models are qualitatively similar.

evolution code (Paxton et al. 2011, 2013) and coupled to the GYRE stellar oscillation code (Townsend & Teitler 2013). This comparison is possible thanks to detected triplets on the one hand, and the almost equally-spaced sequence of dipole g modes with consecutive order as theoretically expected for such modes on the other hand. The radial orders matching the observations range from  $n = 32$  to  $n = 14$ .

Most of the 19 dipole modes of KIC 10526294 reveal a very narrow rotationally-split triplet structure. If we assume that the *cyclic* rotation frequency, which we denote as  $\Omega$ , depends on the radial coordinate  $r$  only, the frequency splitting of a mode with degree  $l$  and radial order  $n$ , denoted as  $\delta_{nlm}$ , can be written as

$$\delta_{nlm} = m\beta_{nl} \int_0^{R_*} K_{nl}(r) \Omega(r) dr, \quad (2)$$

where the unimodular mode kernel  $K_{nl}(r)$  is a function of the mode’s displacement ampli-

tudes  $\xi_r(r)$  (vertical) and  $\xi_h(r)$  (horizontal), while  $\beta_{nl}$  is given by

$$\beta_{nl} = \frac{\int_0^{R_*} [\xi_r^2 + l(l+1)\xi_h^2 - 2\xi_r\xi_h - \xi_h^2] r^2 \rho dr}{\int_0^{R_*} [\xi_r^2 + l(l+1)\xi_h^2] r^2 \rho dr}$$

and is connected with the Ledoux splitting as  $\beta_{nl} = 1 - C_{nl}$  (e.g., Aerts et al. 2010, Chapter 3). The rotationally-induced splittings for the 19 detected modes are shown in Fig. 1 (top panel, adapted from Fig. 8 in Pápics et al. (2014)), together with the mode periods derived from Model 1 and Model 2 (bottom panel). The mode kernels for both models are shown in Fig. 2 and their squared Brunt-Väisälä frequency  $N^2$  is shown in Fig. 3. The latter illustrates the slightly more advanced stage of Model 1 compared to Model 2.

Some of the observed splittings are not symmetric with respect to the central  $m = 0$  peak. These asymmetries are usually related to mechanisms capable of lifting partially the  $2l + 1$  degeneracy of a given multiplet, such as deviations from sphericity or large-scale magnetic fields. We assume to be dealing with a physical phenomenon that causes asymmetries without lifting the degeneracy between the retrograde ( $m < 0$ ) and prograde ( $m > 0$ ) modes. Rotationally-induced splittings as expressed by Eq. (2) are only capable of lifting the  $\pm m$  degeneracy. Hence, forward modeling including only differential rotation up to first order cannot fully capture these observed asymmetries. On the other hand, Eq. (2) is still perfectly valid even in the presence of mechanisms mentioned above, with the caveat that it then accounts for one-half of the splitting between the  $+m$  and the  $-m$  modes and not for the splitting between a mode with a given  $m$  and the corresponding central  $m = 0$  peak. It is known that the presence of a magnetic field near the convective core, as discussed by Hasan et al. (2005), can give rise to such effects. In fact, the mode kernels considered here have substantial amplitudes precisely in that zone, making them particularly susceptible to this effect. Given that we have no information on the presence or absence of a magnetic field in KIC 10526294, we will address only the symmetric components of the splittings in this study, assuming rotation to be the dominant mechanism responsible for the observed splittings and

Table 2. Fundamental stellar parameters of KIC 10526294 from the best matching theoretical model (Model 1) found by Moravveji et al. (2015) and by Pápics et al. (2014) (Model 2).

Model	$T_{\text{eff}}$ [K]	$M_*/M_\odot$	$R_*/R_\odot$	$f_{ov}$	$Z$	$X_c$	Age [Myr]	$\chi^2$
1	13000	3.25	2.215	0.017	0.014	0.627	63	1.42
2	12470	3.20	2.100	< 0.015	0.020	0.693	12	10.9



leaving the modeling of the asymmetries for a future more specialised study. As explained earlier, the presence of the asymmetries leads to increased errors in the splittings.

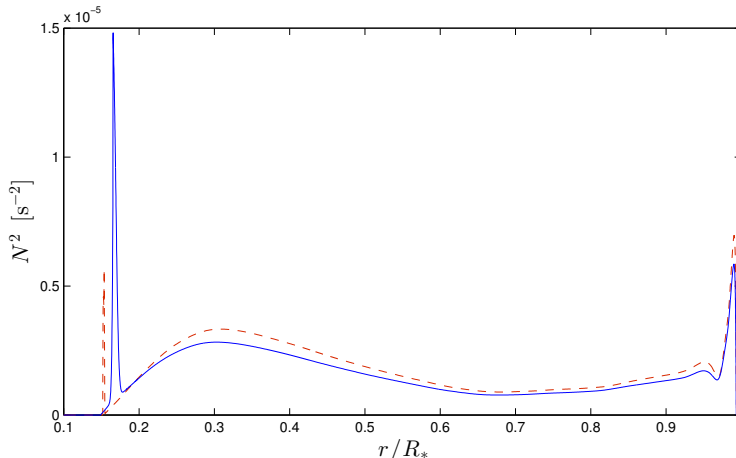


Fig. 3.— The squared Brunt-Väisälä frequency  $N^2$  as a function of stellar fractional radius for the best model from Moravveji et al. (2015) (continuous blue curve) and for the best model from Pápics et al. (2014) (red-dashed curve). The larger peak of the former model near the core boundary (at  $r \sim 0.15 R_*$ ) is comparatively further away from that boundary than the peak of the latter model, thus allowing some modes to be “trapped” between the core boundary and the peak. See also Fig. 2.

### 3. Cumulative kernel integrals

Each mode samples differently the internal rotation of the star. This is usually illustrated by plotting the cumulative integral of the kernels  $K_i$ . For increased contrast we plot instead in Fig. 4 the cumulative integral of  $k_i(r)$ , which we define by

$$k_i(r) = K_i(r) - \langle K(r) \rangle, \quad (3)$$

where  $\langle K(r) \rangle$  is the average of the kernels across modes at each radius  $r$ . This  $\langle K(r) \rangle$  is the ‘common’ kernel and its integral will only contribute to the average of the splittings. Similarly we can express a given profile  $\Omega(r)$  as a sum of its mean value  $\bar{\Omega}$  (across the radial coordinate), plus a fluctuating part  $\omega(r)$  (with zero mean):

$$\Omega(r) = \bar{\Omega} + \omega(r). \quad (4)$$

Therefore we can write the *scaled* splittings as:

$$\Delta_i = \frac{\delta_{nlm}}{m\beta_{nl}} = \bar{\Omega} + \int_0^{R_*} \langle K(r) \rangle \omega(r) dr + \int_0^{R_*} k_i(r) \omega(r) dr. \quad (5)$$

The first two terms on the right hand side comprise the average splitting, while differences

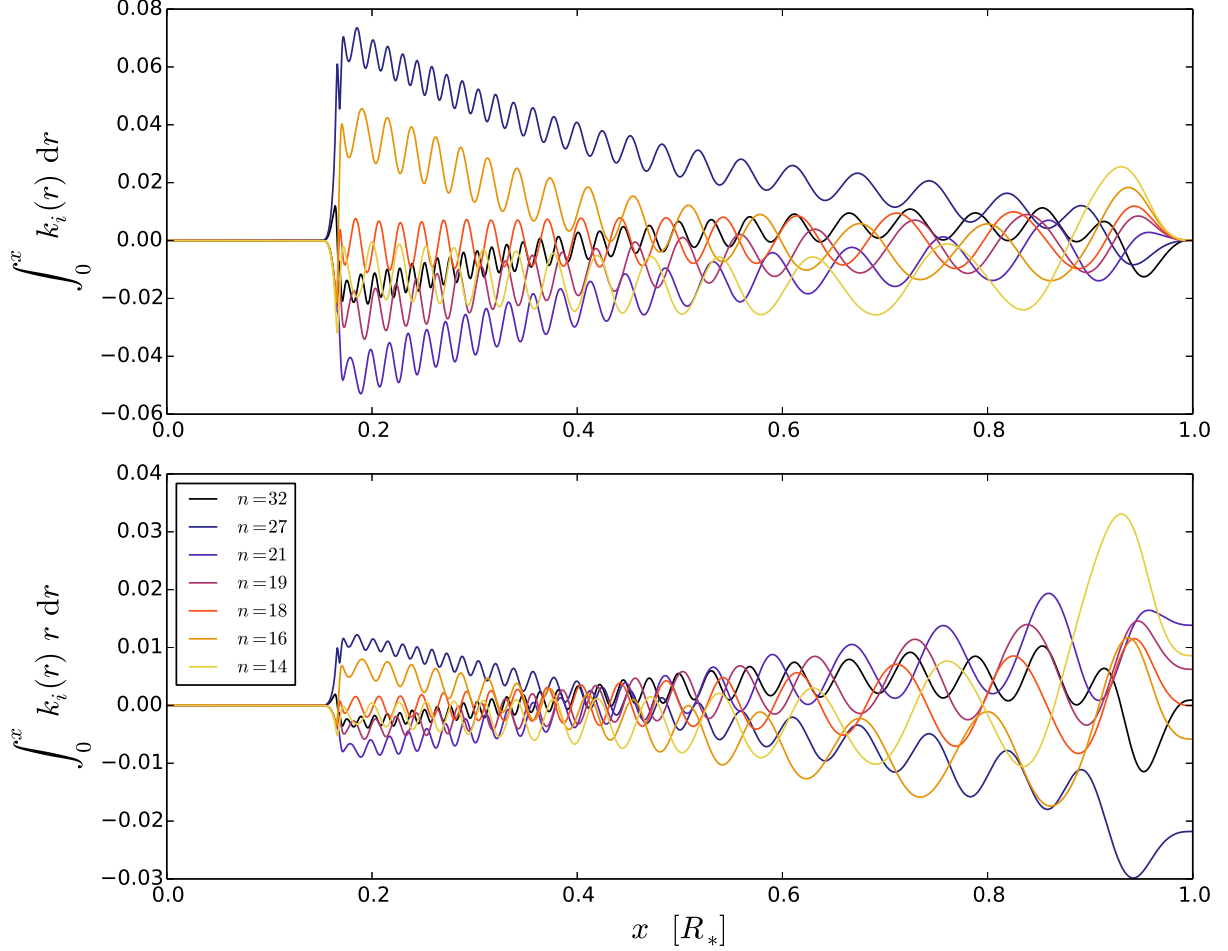


Fig. 4.— Cumulative integrals of  $k_i(r)$  (top) and  $r k_i(r)$  (bottom) for a sample of dipole ( $l = 1$ ) modes from Model 1 with various degrees of trapping. Mode with  $n = 27$  is the “most” trapped near the core as compared with the  $n = 21$  which is the “least” trapped.

across modes come into play in the last term. Figure 4 shows the cumulative integrals of  $k_i(r)$  and of  $k_i(r) r$  for a sample of modes from Model 1 with various degrees of trapping near the core. From the figure it is evident that the “least” trapped mode (the one with  $n = 21$ ) would have the largest splitting in response to a rotation profile that increases linearly with radius. Conversely, the “most” trapped mode near the core ( $n = 27$ ) would have the smallest splitting under the same condition.

#### 4. Trapped modes and linear rotation profiles

Here we follow closely the analysis done by Kawaler et al. (1999) for g modes in white dwarf pulsators. We take advantage of the fact that some modes are trapped as revealed by the kernel amplitudes. They are trapped very close to the overshooting zone while other modes have more spread-out amplitudes, comparatively. This trapping manifests itself as reduced period spacings if we plot them as functions of period (Kawaler & Bradley 1994). The observed spacings of KIC 10526294 are shown in Fig. 5 together with the *scaled* splittings  $\delta_{nlm}/m\beta_{nl}$  (see Eq. 2). A linear fit to the scaled splittings results in a slope of 27.04 nHz/( $10^5$ s) and an intercept of 26.20 nHz.

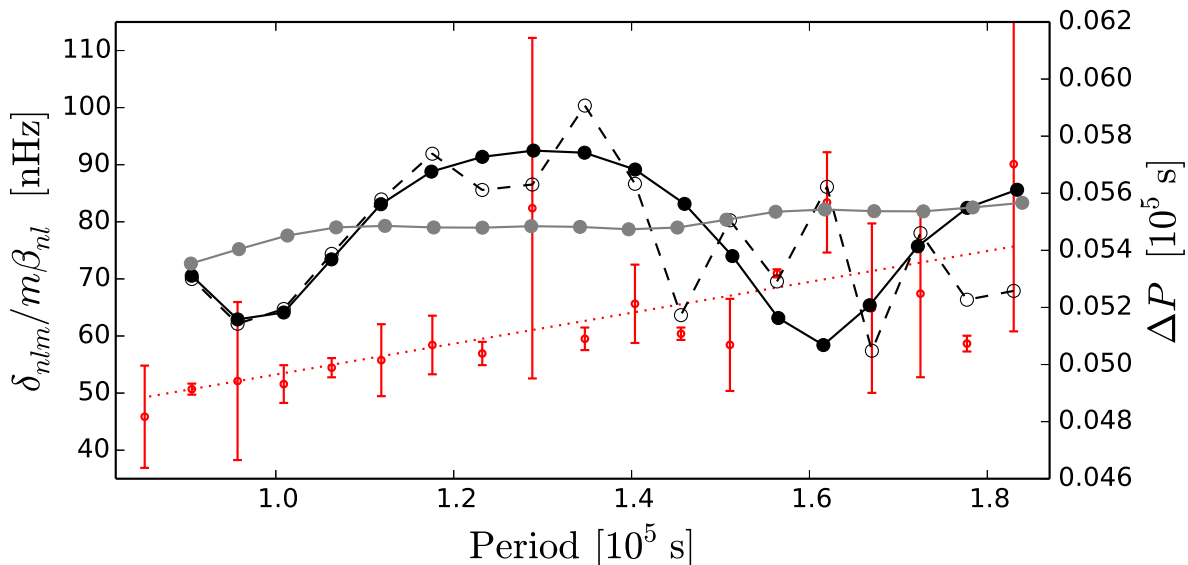


Fig. 5.— The scaled rotational splittings  $\delta_{nlm}/m\beta_{nl}$  deduced from the observations (red error bars) as a function of the mode period together with a linear fit (dotted red line, slope: 27.04 nHz/( $10^5$ s), intercept: 26.20 nHz, scale is on the left). The dashed line connects the observed period spacings defined as  $\Delta P_n = \Pi_n - \Pi_{n-1}$ . The black continuous line connects the spacings derived from the seismic Model 1 in Table 1 while the grey continuous line connects the spacings derived from Model 2. (scale is on the right). The trapped modes of Model 1 are those with periods close to  $0.95 \times 10^5$  s and  $1.6 \times 10^5$  s.

Let us now do forward modeling to find the predicted splittings using synthetic, linear rotation test profiles. Two test profiles have  $\Omega = 5$  nHz at  $r = 0$  and have the same slope in absolute value,  $1 \text{ nHz}/R_*$ , but opposite in sign. The results are shown in Fig. 6, where the top and bottom plots correspond to increasing and decreasing rotation profiles, respectively.

We see the clear signature of mode trapping. Trapped modes are closer to the core, so if the rotation profile increases with radius, then the corresponding splittings are comparatively smaller. Analogously, if the rotation decreases with radius then the trapped modes will show comparatively larger splittings than the other modes. The latter situation is precisely what we can see in Fig. 6. A similar situation occurs for the white dwarf PG 1159-035, as

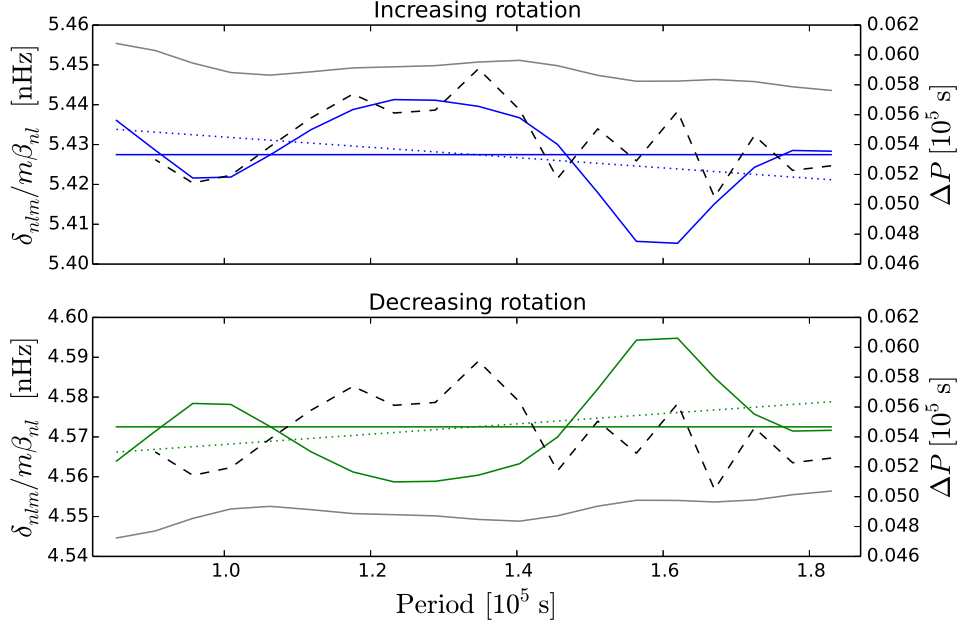


Fig. 6.— Top: the scaled rotational splittings for a linearly increasing rotation profile derived from Model 1 and 2 (continuous blue and grey curves, respectively), the blue dotted line is a linear fit to the splittings from Model 1, scale is on the left. Bottom: the splittings for a linearly decreasing rotation profile derived from both Model 1 and 2 (continuous green and grey curves, respectively), the green dotted line is a linear fit to the splittings from Model 1, scale is on the left. For comparison, the horizontal lines show the splittings from constant rotation profiles having the same mean splittings as the splittings from the increasing or decreasing profiles (top, blue horizontal line and bottom, green horizontal line, respectively). The black dashed lines on both plots show the period spacings from observation, scales are on the right.

reported by Kawaler et al. (1999), the only difference being that some modes in the white dwarf are trapped close to the surface such that the results are reversed compared to those for KIC 10526294.

This simplified analysis is helpful because it gives a first idea of the sign of the slope of an unknown rotation profile just by plotting the splittings and the period spacings and see if

they vary in phase. In our case it is not very clear if they vary in phase or not, so instead we make use of the linear trends of the splittings as indicated with the linear fits (dotted lines) in Fig. 6. When period spacings and splittings vary in phase, the linear trend is downward (negative slope). Conversely, when period spacings and splittings are in anti-phase, the linear trend is upward (positive slope). The observed splittings of KIC 10526294 have an *increasing* trend, as evidenced by the linear fit (dotted red line) in Fig. 5. We associate this with a *decreasing* rotation rate.

We can now do a simple calculation to estimate the optimal slope  $a$  of a linear rotation profile  $\Omega(r) = ar + b$  that best matches the observed *slope*. We assume that the slope of the fit to the measured splittings is linear with respect to the slope of the rotation profile, which seems to be the case. The *ratio* of the linear slopes associated with the observed splittings and the splittings of the linearly decreasing test profile discussed above is  $\sim 2.0918 \times 10^3$ . Therefore, if we use a linearly decreasing rotation profile with a slope of  $2.0918 \times 10^3$  times the original slope of our (linearly decreasing) test profile and adjust its mean level to match the *mean* of the observed splittings, we might get an idea of the underlying rotation profile. The slope we obtain in this way is  $a \sim -2.0918 \mu\text{Hz}/R_*$ . Adjusting the slope of the test profile so as to match the trend of the observed splittings also requires adjusting  $b$  according to Eq. (6) if we are to match the average of the observed splittings. We calculate the intercept  $b$  as (see also Eq. 5)

$$b = \langle \delta \rangle - a \int_0^{R_*} \langle K(r) \rangle r \, dr, \quad (6)$$

where  $\langle \rangle$  denotes the average over all modes, and get  $b \sim 0.957 \mu\text{Hz}$ . These values of  $a$  and  $b$  imply that part of the rotation profile becomes negative. Hence, in the case that the splittings are actually caused by a linear rotation profile or any other profile closely resembling a linear one, we deduce that the mean observed splittings should have been considerably higher in magnitude in order to obtain a rotation profile that would not include counter-rotation inside the star. Of course, with this exercise, we were only trying to match the *linear trend* and the *mean* of the observed splittings through a linear test profile. In this case the *rms* deviation of the predicted splittings from the observed ones is around 22.42 nHz, comparatively large compared to the mean error from the observations which is 8.41 nHz (scaled, from Error Set 1). We can make use as well of the *reduced*  $\tilde{\chi}^2$  values which we compute throughout this work as

$$\tilde{\chi}^2 = \frac{\chi^2}{\nu} = \frac{1}{\nu} \sum_{i=1}^M \left( \frac{\bar{\delta}_i - \delta_i}{\epsilon_i} \right)^2, \quad (7)$$

where  $\delta_i$  and  $\bar{\delta}_i$  are the measured and predicted splittings, respectively,  $\epsilon_i$  are the errors,  $\nu$  is the *effective* number of degrees of freedom and  $M$  is the number of observed splittings. In the case just discussed above we fitted two parameters,  $a$  and  $b$ , so the number of degrees of

freedom is  $\nu = M - 2 = 17$  which leads to  $\tilde{\chi}^2 \sim 194.8$ .

Figure 7 presents another hint towards the decreasing rotation as the radius increases. We plot the observed splittings as a function of  $\int_0^{R_*} k_i(r) r dr$ , where  $k_i(r)$  is defined in Eq. (3). This should have been a straight line with negative slope if the splittings were actually caused by a linear rotation profile. As the figure shows, the splittings have an overall downward trend which is a rough indication that the rotation profile decreases as we move towards the star’s surface.

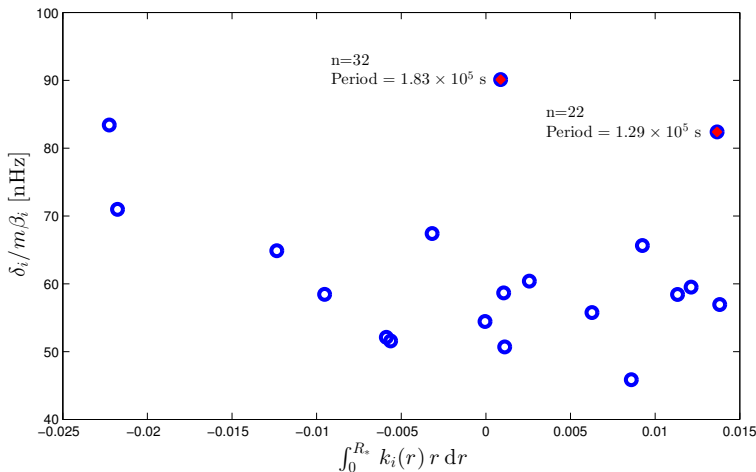


Fig. 7.— The observed splittings (scaled) as a function of  $\int_0^{R_*} k_i(r) r dr$ . Even considering the two splittings marked in red (which are coincidentally the ones with largest errors), there is a downward trend which hints at decreasing rotation as the radius increases.

In a next exercise, we searched for the linear profile that minimizes  $\tilde{\chi}^2$ . This profile has a slope of  $a = -530.7 \text{ nHz}/R_*$  and an intercept  $b = 285.1 \text{ nHz}$ , leading to  $\tilde{\chi}^2 = 6.74$ . This profile again leads to negative values for the rotation frequency in the outer envelope. To have an idea of the comparative statistical significance of this result, we computed the optimal *constant* rotational profile, as well as the optimal linear profile *restricted to positive values* (using a Lagrange multiplier as an additional fitting parameter). We obtained  $\tilde{\chi}_{\text{const}}^2 = 19.86$  and  $\tilde{\chi}_+^2 = 16.86$ , respectively. None of the positive linear rotational profiles have a  $\tilde{\chi}^2$  similar to the linear profile with counter-rotation.

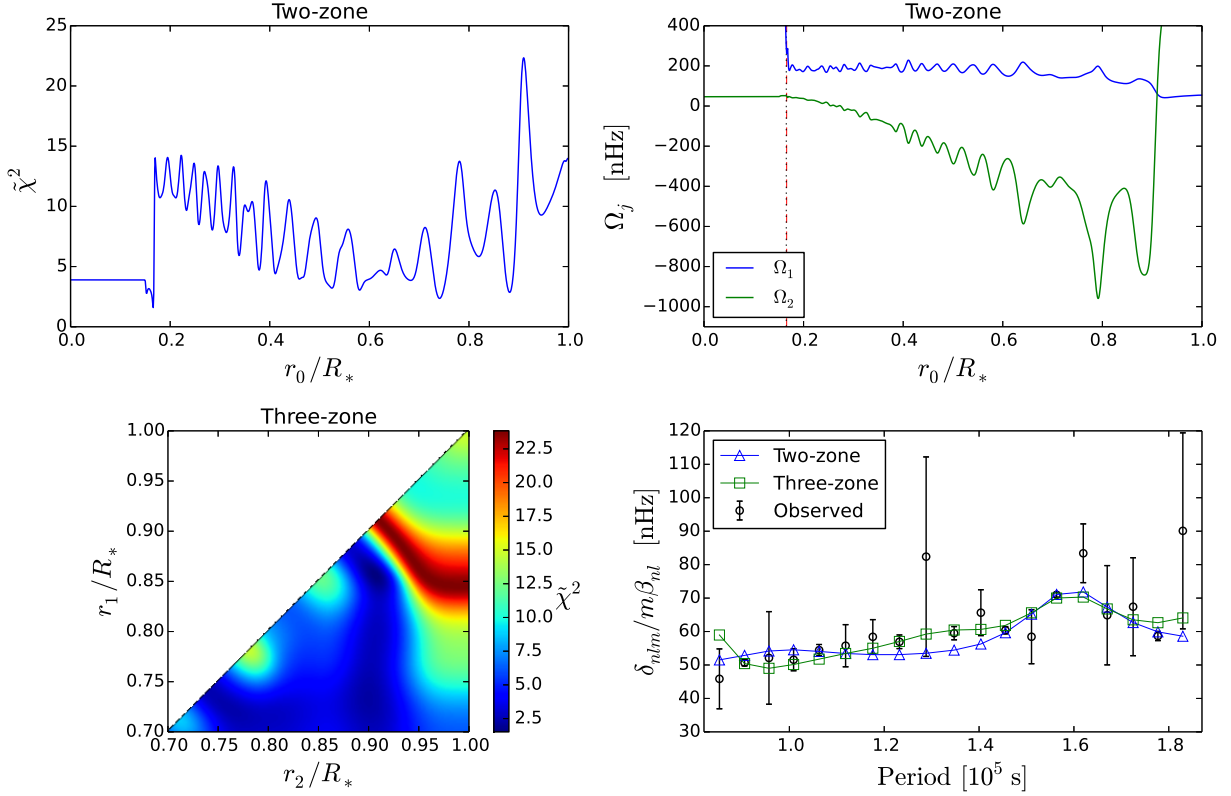


Fig. 8.— Top left:  $\tilde{\chi}^2$  from the difference between the predicted and observed splittings as a function of the two-zone parameter  $r_0$ . Top right: the values of  $\Omega_1$  (blue) corresponding to  $r < r_0$  and  $\Omega_2$  (green) for  $r > r_0$ , both as functions of  $r_0$ . The vertical dotted line in black indicates the extent of the core and the overshoot region, it coincides closely with the optimum  $r_0$ . Bottom left:  $\tilde{\chi}^2$  computed from a three-zone model with  $r_1$  and  $r_2$  as parameters. The lowest  $\tilde{\chi}^2$  is achieved when  $r_1 = 0.85 R_*$  and  $r_2 = 0.91 R_*$ . Bottom right: Observed and predicted splittings from the two-zone model together with the predicted splittings corresponding to the lowest  $\tilde{\chi}^2$  from the three-zone model (green squares).

## 5. Linear, piece-wise rotation models

We now assume a two-zone, piece-wise rotational profile such that its value is  $\Omega_1$  if  $0 < r < r_0$  and  $\Omega_2$  if  $r_0 < r < R_*$ . The parameter  $r_0$  is variable and we optimize  $\tilde{\chi}^2(r_0)$  so as to best match the observations, whose errors are derived from Error Set 1. The resulting  $\tilde{\chi}^2$  versus  $r_0$  is shown in the top left panel of Fig. 8. The minimum occurs at  $r_0 \sim 0.166 R_*$ . The values of  $\Omega_1, \Omega_2$  are shown as functions of  $r_0$  in the top right panel of Fig. 8. The bottom right panel of Fig. 8 shows the observed splittings (scaled) and the splittings for the

two-zone model with the minimum at  $r_0 = 0.166 R_*$ , corresponding to  $\Omega_1 = 262.71$  nHz and  $\Omega_2 = 49.33$  nHz. We note that the boundary of the convective core of Model 1, extended with the core overshoot zone, is situated at  $0.1652 R_*$  (Moravveji et al. 2015). The second deepest minimum in the top left panel of Fig. 8 occurs at  $r_0 = 0.741 R_*$  and corresponds to  $\Omega_1 = 142.0$  nHz and  $\Omega_2 = -418.2$  nHz; this solution leads to an  $r_0$  that does not play a special role in Model 1 in terms of physical quantities.

The two-zone model thus favors a region rotating with a period of 42 d near the core overshoot zone and a co-rotating envelope with a period of 254 d ( $\tilde{\chi}^2 = 1.59$ ). The second minimum has  $\tilde{\chi}^2 = 2.36$  and corresponds to a counter-rotating profile. The averaging kernels (for a definition, see Section 6) associated with the best two-zone model are presented in Fig. 9 and reveal that the outer zone averaging kernel probes mostly the radiative envelope, while the inner zone averaging kernel exhibits a large maximum just before reaching the core-envelope boundary and rapid oscillations around zero away from it.



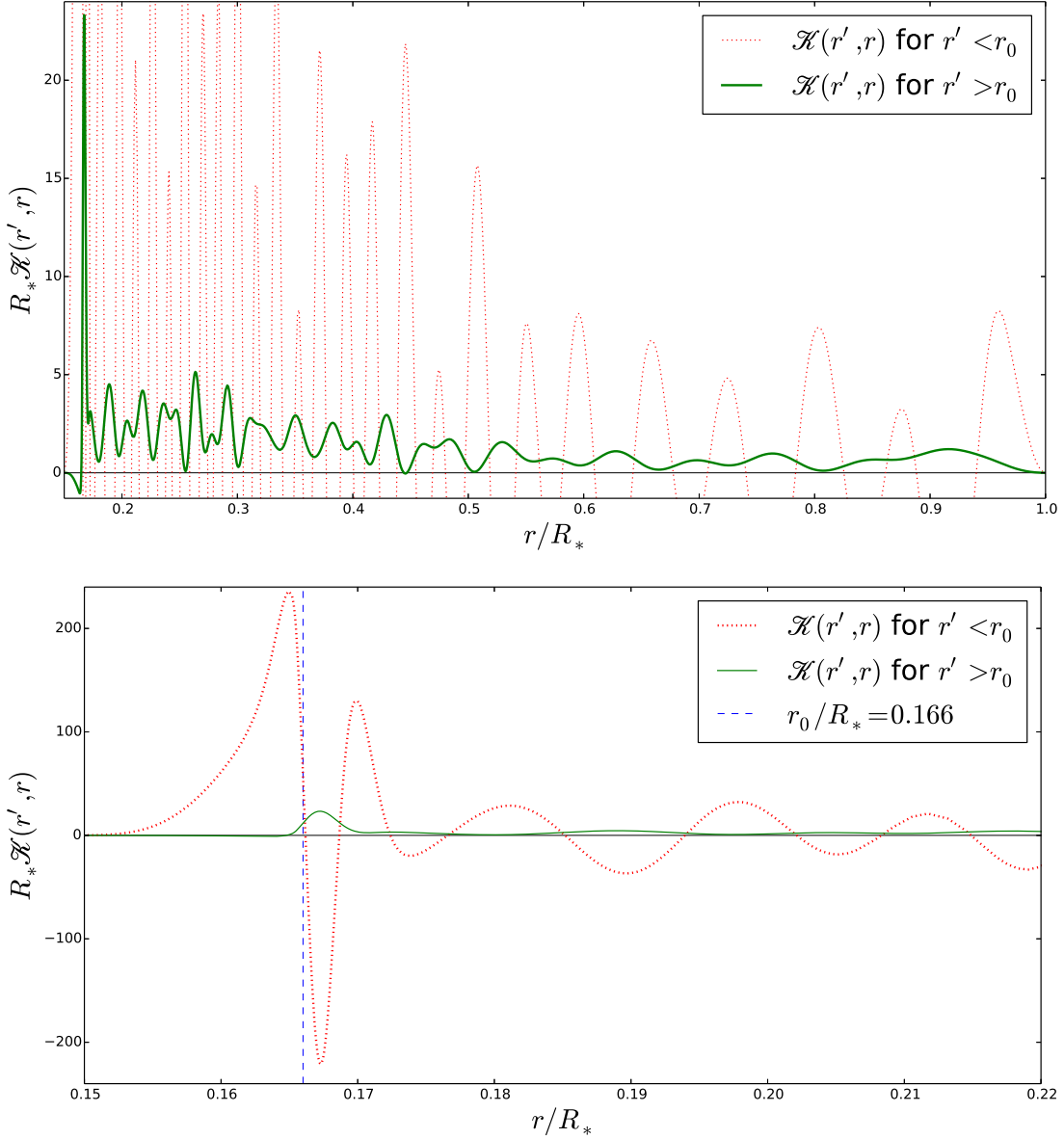


Fig. 9.— Top: averaging kernels  $\mathcal{K}(r', r)$  of the optimum two-zone model with a discontinuity at  $r_0/R_* = 0.166$ . Bottom: zoom on the core-envelope boundary region.

A slightly more complex version of this two-zone model is implemented by introducing a third middle zone where the rotation profile changes linearly from  $\Omega_1$  at the end of the inner zone to  $\Omega_2$  at the start of the outer zone. In this case, we have two linear parameters  $\Omega_1, \Omega_2$  and two non-linear parameters  $r_1, r_2$  defining the zone boundaries. The lowest  $\tilde{\chi}^2 = 1.51$  for this three-zone model is achieved when  $r_1 = 0.85 R_*$  and  $r_2 = 0.91 R_*$  (see bottom left

panel of Fig. 8) and indicates counter-rotation ( $\Omega_1 = 151.8 \text{ nHz}$ ,  $\Omega_2 = -1069.5 \text{ nHz}$ ). The corresponding splittings are also shown in the bottom right panel of Fig. 8.

Very similar results are obtained when the uncertainties are derived from Error Set 2 or when the most asymmetric modes are excluded as evidenced by Figs. 19 through 21. All the three-zone  $\tilde{\chi}^2$  minima in the four cases, i.e., using Error Set 1 or 2 and with or without the most asymmetric splittings, correspond to cases with counter-rotation. According to their  $\tilde{\chi}^2$  values, these three-zone models have a statistical significance comparable with the best two-zone model. However, the position of their discontinuities  $r_1$  and  $r_2$  have no obvious physical meaning.

To estimate the performance of different models, with the aim to choose the best one in a statistical sense, one can only rely on likelihood ratios in the case of *nested* models, i.e., for models where all terms of a simpler model version also occur in a more complex version of the model (e.g., Hastie et al. 2009). We are not in such a situation here because we wish to compare linear, discontinuous linear multi-zone, and continuous non-linear inversion profiles (the latter will be discussed in the next Section). In such a case of non-nested models, an adequate statistical measure for model selection is the Akaike Information Criterion (AIC), which assigns a score to a given model rewarding goodness-of-fit (e.g., as measured by  $\chi^2$ ) but penalizing overfitting, thus discouraging the use of complex models with too many adjustable parameters (Burnham & Anderson 2002; Hastie et al. 2009). For our purposes, having only a relatively small number of measurements ( $M = 19$ ), it is appropriate to use the *corrected* AIC, denoted AICc, which we define according to its common use in the literature (e.g., Hurvich & Tsai 1989):

$$\text{AICc} = 2k + \chi^2 + \frac{2k(k+1)}{M-k-1}, \quad (8)$$

where  $k$  is the number of parameters to fit and  $M$  is the number of observations. As advocated by Burnham & Anderson (2002),  $k$  should include the variance of the residuals as a parameter to be fitted, e.g.  $k = 3$  for a linear regression. With this definition,  $k = M - \nu + 1$ . The preferred model among a set of models is the one with the lowest AICc value, where we limit proper model comparison to the case  $M - k > 1$ . These AICc values are only intended for model inter-comparison and have no absolute meaning by themselves. Table 3 lists all the rotation models considered in this work together with some of their associated statistical measures, including their AICc's. Similar tables based on Error Set 2 or by avoiding the most asymmetric splittings, are given in Appendix A. We can see from the AICc values in Table 3 that the two-zone piece-wise model outperforms the three-zone model.

We end this Section by noting that the overall spectral line broadening of  $18 \text{ km s}^{-1}$  measured for KIC 10526294, which is the combination of rotational and pulsational broadening (Pápics et al. 2014), is compatible with all the  $\Omega_2$ -values found from the minima listed in

Table 3. Comparison of rotation profiles for Model 1 (except for one entry, where we used Model 2). The profiles marked with + are enforced to be positive-definite. The effective number of degrees of freedom  $\nu$  for the inversions were computed as  $M - \kappa$ , where  $\kappa$  is trace of the ‘hat’ matrix  $\mathbf{GC}^\top$  (see Section 6), following the same approach as Deheuvels et al. (2014) and explained in Hastie et al. (2009). Error Set 1 is used here.

Rotation Profile	<i>rms</i> error [nHz]	$\nu$	$\tilde{\chi}^2$	AICc
Constant	11.63	18.00	19.86	362.3
Linear	12.32	17.00	6.74	122.1
Linear+	11.46	16.00	16.86	280.7
Two-zone	10.88	16.00	1.59	36.36
Three-zone	9.48	15.00	1.51	37.35
RLS, $N = 8$	9.31	14.43	0.52	24.52
RLS, $N = 14$	10.46	14.32	1.44	38.18
RLS, $N = 8$ (Model 2)	11.35	14.74	6.42	110.3
RLS+, $N = 8$	12.05	10.43	17.16	222.2
RLS+, $N = 14$	11.09	5.32	3.07	184.3
SOLA, $N = 8$	9.77	12.64	0.58	33.59
SOLA, $N = 14$	8.19	9.28	0.45	60.11

this Section and does not allow any discrimination among those solutions as it was the case for the subgiant studied by Deheuvels et al. (2012). In the following, we investigate rotation profiles obtained from inversion methods.

## 6. Inversions

We first introduce the basic concepts and terminology behind the inversion approaches we applied. We are interested in the approximate determination of  $\Omega(r)$  based on a set of observed rotational splittings  $\delta_{nlm}$ , see, e.g., Gough (1985) for one of the earliest applications of this method in the solar case and Kawaler et al. (1999) and Deheuvels et al. (2012) for applications to white dwarfs and subgiants, respectively. This constitutes a linear problem and the approximate solution  $\bar{\Omega}(r)$  can be written as

$$\bar{\Omega}(r) = \sum_{i=1}^M c_i(r) \Delta_i, \quad (9)$$

where  $\{i\}$  represents the collective index  $\{nlm\}$ ,  $\Delta_i \equiv \delta_{nlm}/m\beta_{nl}$  are the scaled splittings,  $c_i(r)$  are the yet-unknown *inversion coefficients*, and  $M$  is the number of observed modes. It is convenient to express the approximate rotational profile  $\bar{\Omega}(r)$  in terms of the true profile  $\Omega(r)$  by means of the *averaging kernels*  $\mathcal{K}(r', r)$ . They are related to the kernels  $K_i(r)$  through  $\mathcal{K}(r', r) = \sum_{i=1}^M c_i(r') K_i(r)$  and fulfill

$$\bar{\Omega}(r') = \int_0^{R_*} \mathcal{K}(r', r) \Omega(r) dr. \quad (10)$$

From the preceding relation it is clear that the averaging kernels  $\mathcal{K}(r', r)$  should be as much as possible localized around  $r'$ , ideally resembling a delta function  $\delta(r', r)$ .

We consider now in what follows a radial grid (scaled with the stellar radius  $R_*$ ) of  $N + 1$  uniformly spaced points  $\{r_0, r_1, \dots, r_N\}$  with  $r_0 = 0$  and  $r_N = 1$ , covering the full range of fractional radius. The goal of the inverse problem is to determine the  $N$  unknowns  $\bar{\Omega}_j$ , which represent the predicted angular velocity  $\bar{\Omega}$  at radius  $r$  such that  $r_{j-1} \leq r \leq r_j$ , where  $j = 1, \dots, N$  is the grid index. This discretization of  $\bar{\Omega}$  on a radial grid allows us to write an expression for the corresponding predicted splittings  $\bar{\Delta}_i$ , based on Eq. (2), as:

$$\bar{\Delta}_i = \sum_{j=1}^N G_{ij} \bar{\Omega}_j, \text{ where } G_{ij} = \int_{r_{j-1}}^{r_j} K_i(r) dr, \quad (11)$$

or simply  $\bar{\mathbf{\Delta}} = \mathbf{G}\bar{\mathbf{\Omega}}$  in matrix form. Analogously, we express Eq. (9) as

$$\bar{\Omega}_j = \sum_{i=1}^M c_{ij} \Delta_i, \quad (12)$$

with the inversion coefficients  $c_{ij}$  constituting the matrix  $\mathbf{C}$ . It is instructive to put the relation above in terms of the discrete version of the *true* rotation profile  $\Omega(r)$ . It is straightforward to show that the matrix  $\mathbf{A}$ , defined through  $\mathbf{A} = \mathbf{C}^\top \mathbf{G}$ , accomplishes such task by fulfilling

$$\bar{\Omega}_j = \sum_{k=1}^N A_{jk} \Omega_k. \quad (13)$$

Ideally  $A_{jk}$  should resemble a Kronecker-delta  $\delta_{jk}$  indicating that the recovered profile at a given radius (specified by the grid index  $j$ ) does not suffer from ‘leakage’ coming from other radial regions. The matrix  $\mathbf{A}$  is thus the discrete equivalent of the averaging kernels  $\mathcal{H}(r', r)$ .

Note that the observed splittings are linearly related to the predicted splittings through the matrix  $\mathbf{G}\mathbf{C}^\top$ , which is known as the ‘hat’ matrix. The trace of this matrix is an estimate of the effective number of adjustable parameters (Hastie et al. 2009, p. 232).

If the observational errors  $\epsilon_i$  are uncorrelated, as we assume here, the variance of the recovered profiles can be estimated as

$$\sigma^2(\bar{\Omega}_j) = \sum_{i=1}^M c_{ij}^2 \epsilon_i^2. \quad (14)$$

The relation above accounts for the errors on the measurements only and its impact on the inversion results; it does not account for the errors inherent to the inversion process itself.

Below we describe two different inversion techniques we used to obtain an approximation to the internal rotation of KIC 10526294, as well as quantitative estimates of the uncertainties originating from the measurement errors.

### 6.1. Regularized least squares method

A technique commonly used in helio- and asteroseismology is the regularized least squares (RLS or Tikhonov) method (e.g., Craig & Brown 1986), which seeks to minimize the quantity  $\mathcal{F}$  defined as

$$\mathcal{F} = \sum_{i=1}^M \frac{(\Delta_i - \bar{\Delta}_i)^2}{\epsilon_i^2} + \mu_{\text{RLS}} \int_0^{R_*} \left( \frac{\partial^2 \bar{\Omega}}{\partial r^2} \right)^2 dr, \quad (15)$$

where  $\Delta_i$  are the observed splittings,  $\epsilon_i$  the corresponding measurement error,  $\bar{\Delta}_i$  are the predicted splittings, and  $\mu_{\text{RLS}}$  is a free parameter (known as the regularization or smoothing

parameter) used to limit the norm of the second derivative on the predicted  $\bar{\Omega}(r)$ . Using our discrete radial grid described earlier, minimization means  $\partial\mathcal{T}/\partial\bar{\Omega}_j = 0$  for all  $j$ . This condition can be written more explicitly using Eq. (11) and Eq. (15) as

$$\mathbf{H}^\top (\mathbf{G}\bar{\Omega} - \mathbf{\Delta}) + \frac{\mu_{\text{RLS}}}{\epsilon_0^2 \delta^3} \mathbf{L}^\top \mathbf{L} \bar{\Omega} = 0, \quad (16)$$

where  $H_{ij} = G_{ij}/\epsilon_i^2$ ,  $\mathbf{L}$  being the discrete second derivative operator,  $\delta$  the radial grid spacing, and  $\epsilon_0^2$  is a scale factor (introduced for convenience) which we set equal to the squared mean of the errors  $\epsilon_i$ . A formal solution is

$$\bar{\Omega} = \left( \mathbf{H}^\top \mathbf{G} + \frac{\mu_{\text{RLS}}}{\epsilon_0^2 \delta^3} \mathbf{L}^\top \mathbf{L} \right)^{-1} \mathbf{H}^\top \mathbf{\Delta}. \quad (17)$$

Obviously, the inverse matrix on the right hand side of Eq.(17) might not exist and in practice we seek a solution in the *least squares sense* instead.

## 6.2. The SOLA method

The Subtractive Optimally Localized Averaging (SOLA) method (Pijpers & Thompson 1994) consists in determining a linear combination of the inversion coefficients  $c_i(r')$  such that the averaging kernels resemble as much as possible a *target function*  $T(r', r)$  while keeping the variance of the predicted profiles,  $\sigma^2(\bar{\Omega})$ , low. To implement this method we minimize

$$\int_0^{R_*} [\mathcal{K}(r', r) - T(r', r)]^2 dr + \frac{\mu_{\text{SOLA}}}{\epsilon_0^2} \sum_{i=1}^M c_i^2(r') \epsilon_i^2 \quad (18)$$

at each  $r'$ , with the constraint  $\int_0^{R_*} \mathcal{K}(r', r) dr = 1$ . In addition to the free parameter  $\mu_{\text{SOLA}}$  we can also adjust the shape of the target function  $T$ . The problem reduces to solving the linear set of  $M$  equations ( $i = 1, \dots, M$  and for each radial location  $r'$ )

$$\sum_{k=1}^M W_{ik} c_k(r') = \int_0^{R_*} K_i(r) T(r', r) dr, \quad (19)$$

where  $W_{ik} = \int_0^{R_*} K_i(r) K_k(r) dr + (\mu_{\text{SOLA}}/\epsilon_0^2) \delta_{ik} \epsilon_i^2$ , together with the constraint  $\sum_k c_k(r') = 1$ . Using the discrete radial grid with  $N$  segments and choosing the target functions as

$$T(r', r) = \begin{cases} N & \text{if } r' \in (r_{j-1}, r_j] \\ 0 & \text{otherwise,} \end{cases}$$

the problem to solve becomes

$$\sum_{k=1}^M \left[ N (\mathbf{G} \mathbf{G}^\top)_{ik} + \frac{\mu_{\text{SOLA}}}{\epsilon_0^2} \delta_{ik} \epsilon_i^2 \right] c_{kj} = N G_{ij}, \quad (20)$$

with the constraint  $\sum_{k=1}^M c_{kj} = 1$ . In this case the target function will approach a Dirac- $\delta$  as  $N$  increases. On the other hand,  $N$  can be low or moderate as long as  $\Omega(r)$  can be assumed not to vary appreciably over a radial segment of the grid.

### 6.3. Profiles from inversion

We present the internal rotation profiles obtained by the two methods described above. For both the RLS and SOLA methods, we scanned different resolutions ranging from  $N = 2$  to 14, each covering a wide range of smoothing parameters  $\mu_{\text{RLS}}$  and  $\mu_{\text{SOLA}}$ , to examine the resulting inversion profiles. To choose the appropriate parameters  $N$  and  $\mu$  is not an easy task and in practice it depends on the *a-priori* information we might have. For example, if we can assume that the rotation profile does not change appreciably over a radial distance  $\lambda$ , then we can safely use a resolution such that  $N = 1/\lambda$ . Alternatively, we can interpret the inversion result as providing information only on those components of the rotation profile that do not change appreciably over a distance  $1/N$ . Generally the higher the change of the profile over a given length scale is, the lower the accuracy of the inversion. If we consider that the rotation profile can be represented as a superposition of profiles with increasing detail (e.g. like a Fourier expansion), then the inversion methods can provide useful information at least on those components that change slowly with radius. Below we discuss the results for the  $N$  values with the best statistical score in terms of the AICc.

We show in Fig. 10 the inversion profiles with  $\mu_{\text{RLS}} = 10^{-5}$  and  $\mu_{\text{SOLA}} = 10^{-2}$ , which represent a good balance between error and resolution for Error Set 1. Similar figures for Error Set 2 and/or ignoring the asymmetric splittings are shown in Figs. 22-24 in Appendix A. We see that both methods give qualitatively similar results for  $N = 8$  and  $N = 14$ . The uncertainty of the SOLA method grows quickly as  $N$  is increased, as opposed to the RLS method. The averaging kernels, as can be judged from Figs. 26 and 27 in Appendix B, are better localized using the SOLA method (as expected, by design), although the uncertainties are somewhat larger compared to the RLS method. The kernels feature larger amplitudes near  $r \sim 0.2 R_*$ , corresponding to small uncertainties at that location. Further out in radius, near  $r \sim 0.9 R_*$ , the uncertainty is larger but the rotation rate is still constrained to be opposite in sign. Note that the kernels provide no information for  $r < 0.15 R_*$  so the inversion results within this radial range have no meaning (cf. Appendix B). An appropriate

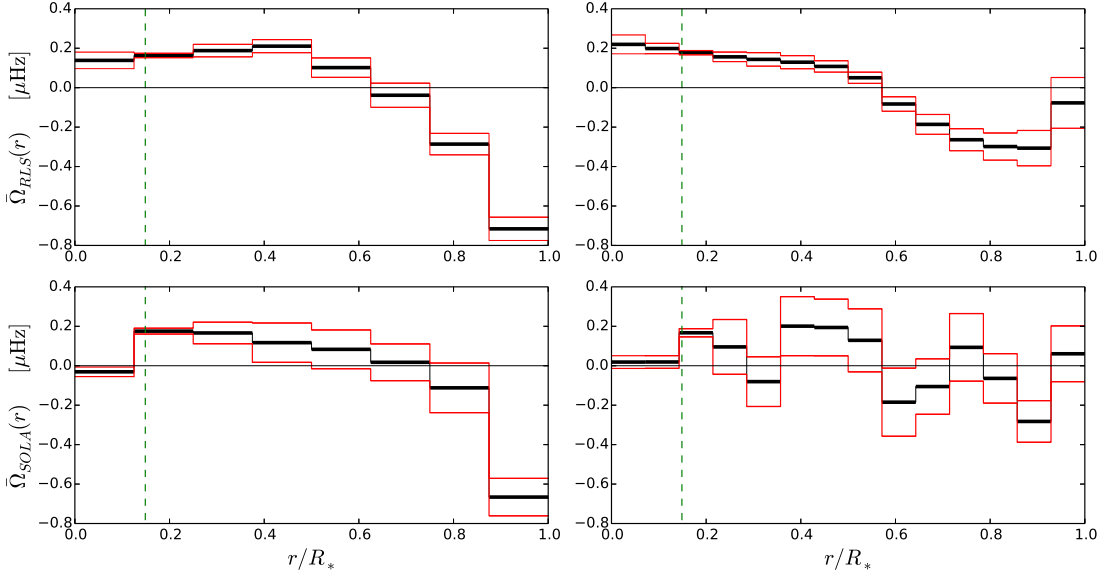


Fig. 10.— Inversion profiles resulting from the RLS method (top row) with  $\mu_{RLS} = 10^{-5}$  and the SOLA method (bottom row) with  $\mu_{SOLA} = 10^{-2}$  for two different resolutions  $N = 8, 14$  (left to right). Vertical dashed lines indicate the approximate location of the convective core’s radius. Error Set 1 has been used.

assessment of the inversion’s accuracy is provided by the averaging kernels, or their discrete counterpart represented by the matrix  $A$  (see Figs. 26 and 27). Generally speaking, as  $\mu_{RLS}$  or  $\mu_{SOLA}$  increases, the predicted splittings  $\bar{\Delta}_i$  will deviate more from the measured ones. The predicted splittings for  $N = 14$  using both RLS and SOLA methods and Error Set 1 is displayed in Fig. 11. The result in the case of the omission of the asymmetric splittings is provided in Fig. 25 of Appendix A.

The best two-zone model from Section 5 might seem in disagreement with the profiles obtained from inversion but upon further inspection they are actually in good agreement, at least for the outer zone. Indeed, if we take the profile from RLS inversion with  $N = 8$ ,  $\mu_{RLS} = 10^{-5}$  and interpolate it appropriately, the resulting average rotation using the outer zone averaging kernel displayed in Fig. 9 amounts to 50.34 nHz, which is in very good agreement with the 49.33 nHz value obtained in Section 5 for the outer zone. The rotation rate computed from the inversion profile and the inner zone averaging kernel amounts to 206.01 nHz, which is to be compared with the 262.71 nHz value for the inner zone in the two-zone model. Although both the best RLS model and the best two-zone are mutually consistent, the RLS model resolves the outer zone better. The AICc values also give preference to the RLS inversions as we deduce from Table 3.



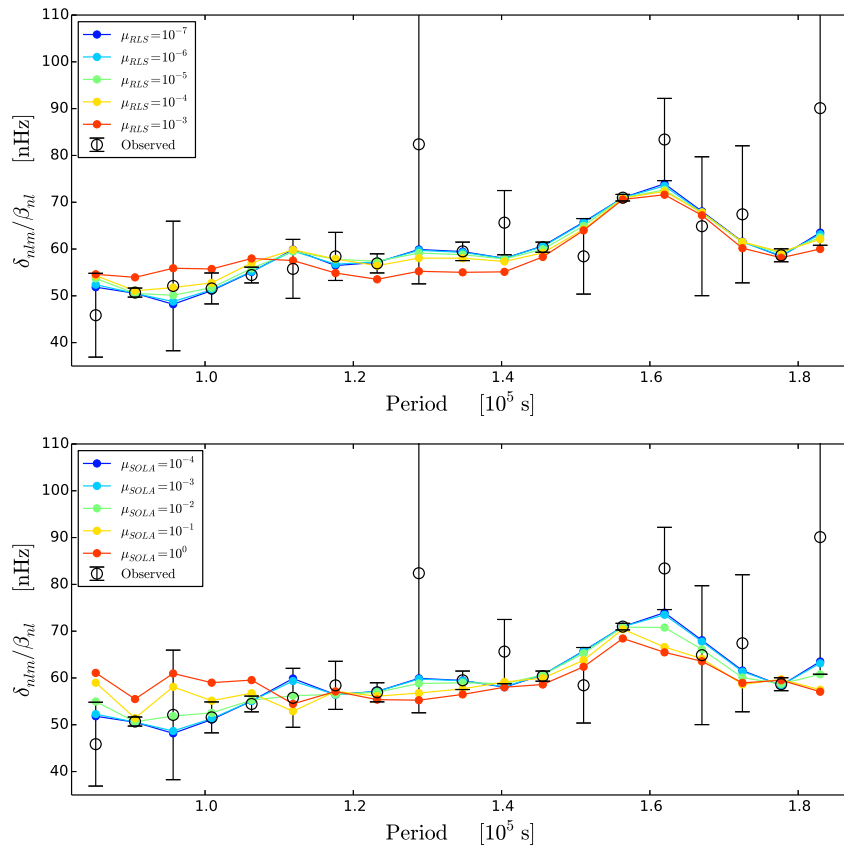


Fig. 11.— The predicted splittings for both the RLS (top) and SOLA methods (bottom) using a resolution of  $N = 14$  and a range of  $\mu$  parameters for each method. The predicted splittings were computed based on the uncertainties from Error Set 1.

To add yet another model comparison, we have performed the so-called leave-one-out cross-validation technique (see e.g. Hastie et al. 2009), which does not rely on  $\tilde{\chi}^2$  values. This technique consists in omitting one of the measurements when fitting a model and comparing the predicted splitting based on the fitted model  $\bar{\Delta}_i$  with the measurement that has been omitted  $\Delta_i$ :  $e_i = (\bar{\Delta}_i - \Delta_i)/\epsilon_i$ . We performed this procedure for each of the measurements at a time and obtained a final score by computing the *rms* value of all the  $e_i$ . The preferred model is then the one with the lowest score. In the case of the two-zone model this score is 1.51 while for the best RLS inversion the score is 0.79.

Using a synthetic profile without counter-rotation as a test, we found that the RLS inversion method works properly and that it is not prone to give spurious counter-rotation solutions. See Appendix D for further details.

It is possible to perform RLS regularized inversions enforcing *a-priori* a rotation profile that does not exhibit counter-rotation. We can achieve this by including additional terms to the quantity  $\mathcal{S}$  defined in Eq. (15) in such a way that they represent our prior knowledge of the rotation profiles being definite positive. Loosely speaking, we can express the probability of obtaining a value  $\Omega_j$  at a given radial location as being proportional to  $e^{\lambda_j \Omega_j}$ , with  $\lambda_j \geq 0$ . A concrete technique to solve such minimization problem is provided by the Karush-Kuhn-Tucker conditions (Kuhn & Tucker 1951), which consists in minimizing  $\mathcal{S} - \sum_j \lambda_j \Omega_j$  together with the constraints  $\lambda_j \Omega_j = 0$  for all radial locations  $j$  (see e.g. Boyd & Vandenberghe 2004). The  $\lambda_j$  are treated as Lagrange multipliers. The result of this exercise is shown in Fig. 12.

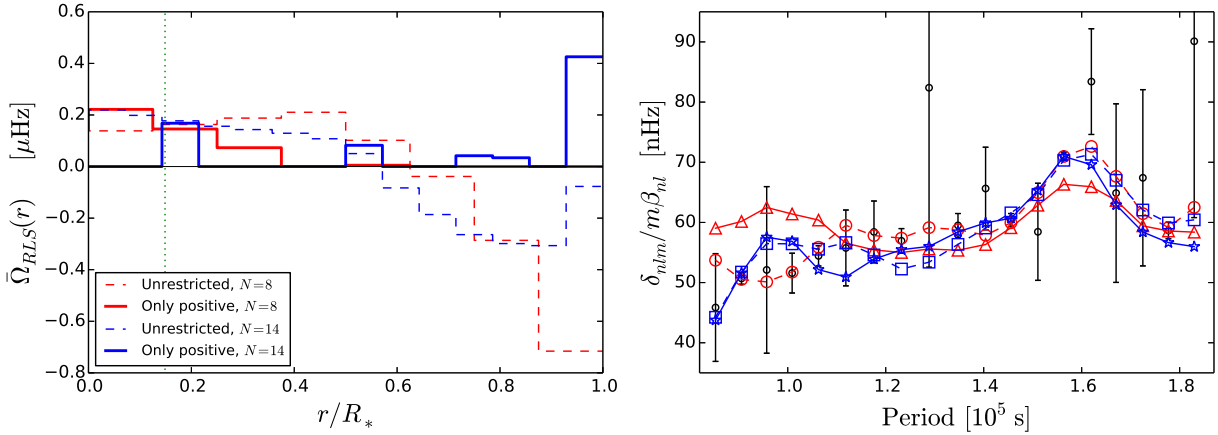


Fig. 12.— Left: comparison of inversion profiles obtained by restricting the rotation to be positive for all  $r$  and those using unrestricted RLS regularization for two different resolutions  $N = 8, 14$  and for  $\mu_{RLS} = 10^{-5}$ . Right: the corresponding predicted splittings compared to observations. See main text for details.

A qualitative idea of how well these restricted-positive profiles represent the data is provided by the plot on the right of Fig. 12. Quantitatively, the  $\tilde{\chi}^2$  for the restricted-positive profiles are  $\tilde{\chi}_{8+}^2 = 112.9$  and  $\tilde{\chi}_{14+}^2 = 46.1$  corresponding to resolutions of  $N = 8$  and  $N = 14$ , respectively. These values are to be compared with  $\tilde{\chi}_8^2 = 0.52$  and  $\tilde{\chi}_{14}^2 = 1.44$  from the unrestricted case. Note here that the effective number of degrees of freedom  $\nu$  is reduced considerably when restricting the profiles to be positive definite given the additional parameters included as Lagrange multipliers. In Table 3 we assembled all the AICc scores of these and other inversions along with results from previous sections.

Although it is possible to increase the resolution  $N$  beyond the number of observations  $M$  without overfitting for the inversion result itself, following the principle of regularization (see Appendix C), the value of  $\nu$  computed as the trace of the ‘hat’ matrix  $\mathbf{GC}^T$  might

become smaller than unity if the regularization parameters are small, pushing the AICc used for model comparison beyond meaningful values. For this reason we limit ourselves to moderate resolutions for the sake of meaningful model comparisons. The best models are the RLS or SOLA inversions with  $N = 8$  with large statistical margin over all the other rotational profiles we obtained.

The profiles obtained using the Error Set 2 (Figs 22 and 24) are very similar to those obtained with Error Set 1. Obviously, the inversion uncertainties are larger but still very similar counter-rotating profiles result. Note that the corresponding  $\tilde{\chi}^2$  and AICc values (Table 4) give clear indication of appreciable error over-estimation in the case of Error Set 2 as already stressed before. Indeed,  $\tilde{\chi}^2 < 1$  in virtually all cases. This is already evident from Fig. 1 where the point-to-point variation of the rotational splittings is visibly much smaller than the average uncertainty from Error Set 2. The inversion profiles are equally unaffected if the inversion procedure is carried out excluding the most asymmetric splittings as evidenced by Figs. 23 and 24. This is not surprising since the large errors associated with the most asymmetric splittings already give them less weight compared to the others when minimizing  $\tilde{\chi}^2$ .

The RLS inversions can be carried out also by regularizing the norm of the first derivative of the profile or even the norm of the profile itself. It turns out they are all consistent and have similar properties as the RLS inversions using the norm of the second derivative that we presented earlier. Figure 13 shows the corresponding inversion profiles and their associated uncertainties derived from the measurement errors.

So far we have based our inversions on the Model 1 found by Moravveji et al. (2015). However, the main qualitative characteristics of the inversion profiles are robust under different model choices. We have explicitly tested that all the models among the best ones from the forward modeling in Pápics et al. (2014) and Moravveji et al. (2015) produce qualitatively similar results for the inverted rotation profiles, i.e., counter-rotation in the radiative envelope. To provide a specific example, we show in Fig. 14 the resulting profile using Model 2 found by Pápics et al. (2014). Although the kernels based on this model do not exhibit a large peak right outside the convective core (i.e., no trapped modes), they have a similar shape otherwise (see also Fig. 3). Again, the inversion profile hints at counter-rotation within the star’s radiative zone. The uncertainty on the recovered profile is somewhat larger overall compared to the uncertainty associated with Model 1 (Fig. 10, top left panel). We attribute this to the lack of variation of the kernels in this model, i.e., there are no trapped modes to make the kernels more ‘different’ from mode to mode. The more similar kernels for the modes of Model 2 result in higher  $\tilde{\chi}^2$  and AICc values, which we have added for the case of RLS and  $N = 8$  in Table 3.

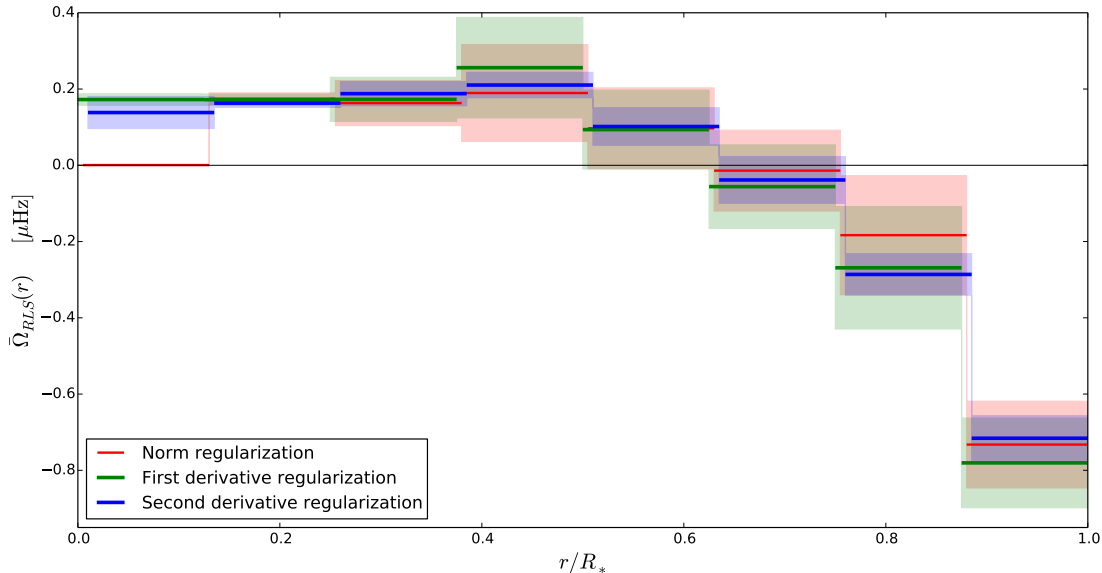


Fig. 13.— The inversion profiles obtained by regularizing the norm of the profile (red,  $\mu_{\text{RLS}}=10^{-6}$ ,  $\tilde{\chi}^2 = 0.53$ ), regularizing the norm of the first derivative (green,  $\mu_{\text{RLS}}=10^{-6}$ ,  $\tilde{\chi}^2 = 0.51$ ) and regularizing the norm of the second derivative (blue,  $\mu_{\text{RLS}}=10^{-5}$ ,  $\tilde{\chi}^2 = 0.52$ ). For visual aid, the profiles have been slightly shifted horizontally with respect to each other.

## 7. Monte Carlo simulations

Yet another method to obtain an approximation to the real profile  $\Omega(r)$  under the assumption of a smooth profile, consists in generating a large collection of random, synthetic test profiles and assigning a score to each measuring how close the predicted splittings are to the observed ones. This method is straightforward but very inefficient computationally since the number of synthetic profiles that need to be calculated is necessarily large.

A random, synthetic profile on a radial grid with  $Q$  points can be generated by choosing a random rotation value  $\Omega_j$  at each radial location  $r_j$ . The rotation values are to be picked from a random (uniform) distribution extending from  $-h$  to  $h$  (in nHz), where the range  $h$  is to be chosen appropriately as described below. In general, such a profile will exhibit strong fluctuations along the radius, i.e. it will be a ‘noisy’ spiky profile, particularly if  $Q$  is large (we used  $Q \geq 100$  in our simulations). There are a number of ways to smooth out the profile, a simple one being to use a ‘low pass’ filter to remove the ‘high frequency’ components of the profile (if we think of it as a time series). The filter cutoff point defines a characteristic length scale  $\lambda$  below which the profile can be considered to have only smooth variations. Some padding at each end of the profile is necessary to avoid end effects when filtering.

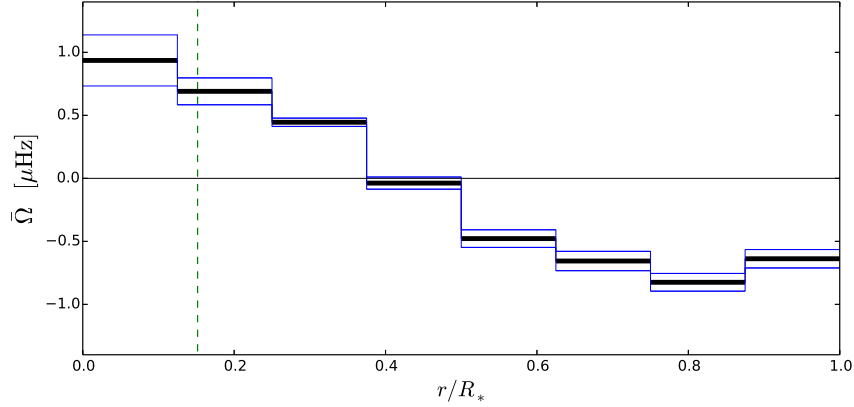


Fig. 14.— The inversion profile obtained using kernels from Model2 as found by Pápics et al. (2014). Here the parameters are identical to those used for the top, left panel in Fig. 10 ( $\mu_{RLS} = 10^{-5}$ ,  $N = 8$ ). The vertical dashed line marks the convective core radius. The counter-rotation within the radiative zone is a characteristic feature of all the models we examined.

See Fig. 15 for an illustrative example. After the smoothing the profile will have spatial

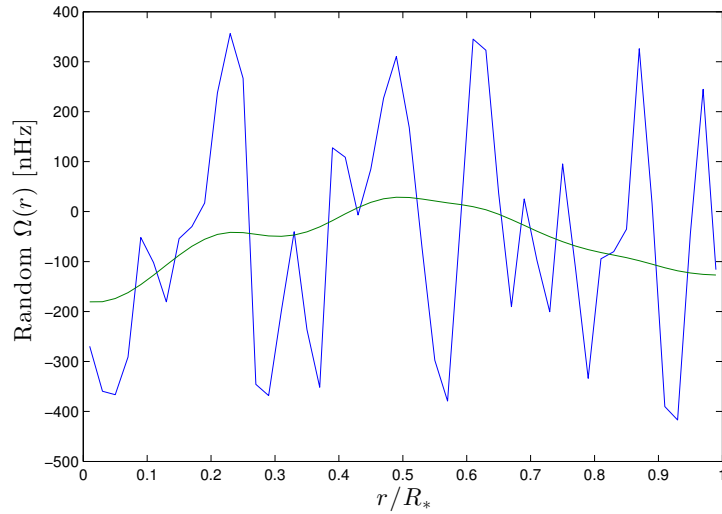


Fig. 15.— A random profile (blue) before any smoothing with  $Q = 100$  and  $h = 500$  nHz. The ‘low pass’ filtering produces the green curve. The correlation length is  $\lambda = 0.3$ .

fluctuations only on length scales larger than  $\lambda$ . Since generally  $Q > N$ , i.e., the random profiles are defined on a finer grid than the one used to define  $\mathbf{G}$ , we should resample the profile to match the radial grid with  $N$  points. We do this by calculating the integral

average of the random profile along each segment in the radial grid associated with  $\mathbf{G}$  after an appropriate interpolation. Other methods can be used to achieve the same result. What is essential here is that the smoothing should be chosen in accordance to the final resolution  $N$  so that  $\lambda N \geq 1$ .

Once the smoothing is performed, the rotation values are not any longer distributed uniformly on the  $[-h, h]$  interval, resembling instead a Gaussian distribution. This is simply because we have introduced short range correlations with our smoothing. Therefore we should adjust the range  $h$  to ensure that the rotation values at a given radial location are more or less equally probable, thus covering uniformly the expected range of  $\Omega(r)$ . This expected range can be roughly estimated from the mean of the observed rotational splittings  $\langle \delta_i/m\beta_i \rangle$ . As a concrete example we found that for  $\lambda = 0.3$  and  $h = 4 \mu\text{Hz}$ , the random profiles visited more or less uniformly the range  $[-0.2, 0.2] \mu\text{Hz}$  within a 14% margin.

If we interpret the rotation value  $\Omega_j$  at each radial location as a random variable, and given a large collection of random rotation profiles, it is possible to calculate the associated covariance matrix. A given row  $j$  of this matrix will resemble a Gaussian distribution centered at  $r_j$ . The mean of the FWHM of the Gaussians in all rows is then an (after-the-fact, of course) estimate of  $\lambda$ . In practice, the random profiles can be considered approximately constant over radial scales not larger than  $\sim \lambda/3$ .

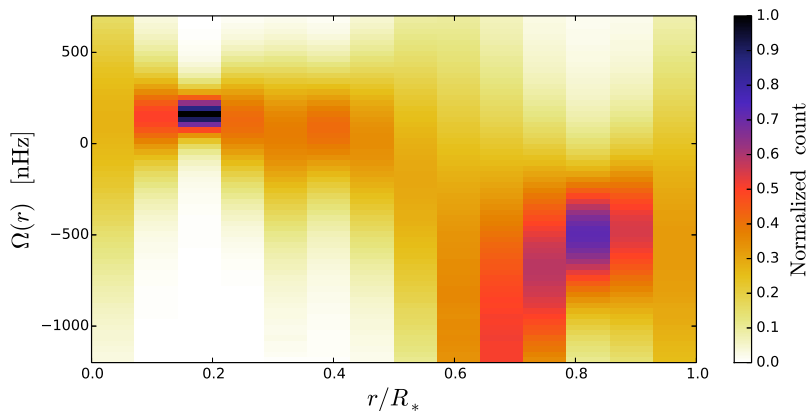


Fig. 16.— Color coded *weighted* histogram count for each radial location of a large sample of random rotation profiles using  $1/\chi^4$  as weights (see text for details). The original random profiles have been smoothed out so that the typical length scale is  $\lambda = 0.3$ .

Once a random profile has been generated and smoothed out, its associated splittings are calculated via Eq. (2). We compute then a score which is proportional to  $\chi^{-4}$  (using Error Set 1). The lower  $\chi^2$  is the higher the score becomes. After scoring a large number of

profiles ( $10^9$ ), we compute the histogram of the rotation rates at each radial location *weighted with their corresponding scores* and then normalized by an ordinary histogram count. In this way, for each radial location and each rotation rate interval we obtain a number indicative of its likelihood to explain the observed splittings.

For the results shown in Fig. 16, the random profiles have a resolution of  $N = 14$  and have been smoothed so that  $\lambda = 0.3$ . At each radial segment  $r_j < r < r_j + 1$  we computed the weighted histogram of the occurrences of  $\Omega_j$  (as explained above) over an interval starting from -1500 up 1200 nHz and subdivided in 71 bins. By comparing Fig. 16 and Fig. 10 we see that the Monte Carlo method reproduces very well the rotation rates at  $r \sim 0.2 R_*$  while giving only a broad distribution of rotation rates centered around negative values at  $r \sim 0.8 R_*$ . We note that virtually none of the high scoring random profiles are strictly positive (or negative), they all involve at least one sign change along the radial coordinate.

This use of random profiles is also suitable to establish the ‘quality’ of a set of kernels. To do this we take first a random profile (the reference profile) and calculate its associated splittings via Eq. (2). These splittings are then ‘inverted’ and we compare the resulting profile with the reference profile. Some random noise could in principle be added to the splittings before attempting the inversion in order to simulate measurement errors, but this is unnecessary here since Eq. (14) already describes properly the effect of the measurement variance on the inversion profiles. The differences between inverted and reference profiles can therefore be attributed solely to the inadequacy of the kernel set to fully recover the solution.

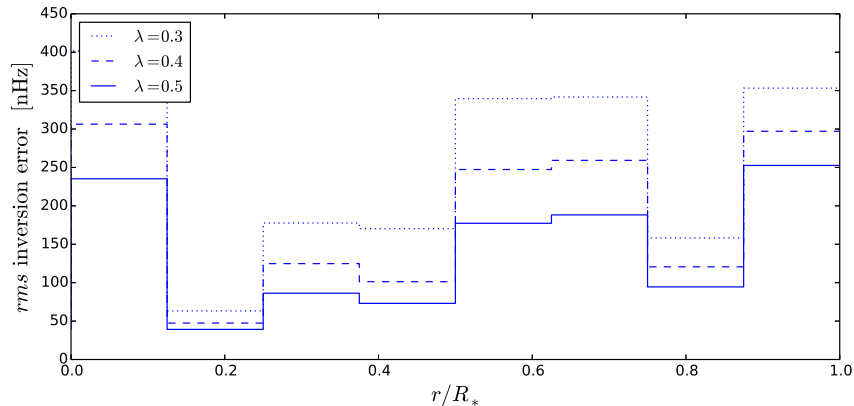


Fig. 17.— *rms* error incurred by RLS inversions with  $\mu_{RLS} = 10^{-5}$  and  $N = 8$  computed from random profiles with various degrees of smoothing. See text for details.

To implement the above, we computed three sets of smooth random profiles ( $\lambda =$

0.3, 0.4, 0.5, respectively and with  $10^6$  profiles each). We then rescaled the amplitude of each individual profile so as to make the corresponding splittings have a mean that equals the mean of the observed splittings. After discarding those profiles whose splittings had mixed signs, we proceeded to perform the inversions ( $\mu_{RLS} = 10^{-5}$ ). We computed inverted profiles with  $N = 8$  intervals of radial resolution and compared them with the reference profiles (integral-averaged over the same radial intervals). The standard errors at each radial interval calculated from all the profiles in the set are shown in Fig. 17. We see clearly that the error becomes larger as the profiles have more variability. The radial locations where the errors are comparatively smaller coincide roughly with the locations where the  $\mathbf{A}$  matrices have better localization (see Fig. 26).

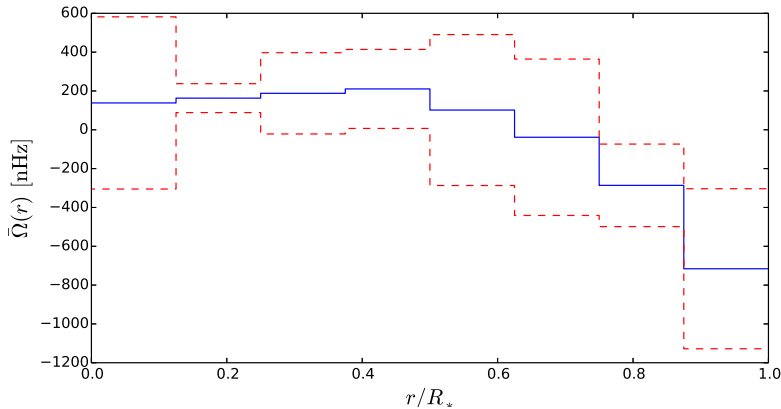


Fig. 18.— RLS inversion profile (solid line) of KIC 10526294 ( $N = 8$ ,  $\mu_{RLS} = 10^{-5}$ ). The error margins incorporate both the measurements errors (from Error Set 1) and the errors related to the inadequacy of the kernels to recover the ‘true’ rotation profile. This latter error was estimated by using smooth random profiles with  $\lambda = 0.3$ .

To conclude this Section we present the inversion profile (from the real KIC 10526294 data) together with an overall ( $1\sigma$ ) uncertainty (derived from both the measurement errors *and* the kernel error as explained above) in Fig. 18. This profile represents a balance between good overall statistical measures and good localization properties, at least near the bottom of the radiative zone and close to the stellar surface. Note that a fully positive rotation profile is possible at  $2\sigma$  level.



## 8. Summary and conclusion

Numerical models and their pulsation properties (based on the MESA evolution code and the GYRE pulsation code) have allowed us to obtain kernels of oscillation modes whose frequencies closely match the identified zonal dipole mode frequencies of the B8V star KIC 10526294 (Pápics et al. 2014; Moravveji et al. 2015). Based on these kernels, we computed rotational profiles explaining the detected rotationally split dipole mode frequencies by assuming different functional forms (constant, linear, two-zone and three-zone). We also performed RLS and SOLA inversions and implemented a Monte Carlo approach to obtain an approximate rotational profile and to estimate the errors incurred by the inversion process. We relied on the optimal equilibrium model found so far for this pulsator (Moravveji et al. 2015) (Model 1) but other seismically derived equilibrium models were also examined and lead to qualitatively similar results.

While the most likely rotation profiles depend on the assumptions made about the functional form of the profile, we were able to constrain the average rotation rate near the overshoot region to be about  $163 \pm 89$  nHz, a value supported by almost all the rotational models we considered. Towards the surface of the star our results are less constrained since they are sensitive to the a-priori assumptions on the shape of the rotational profile. If a smooth and continuous profile is assumed, our results point to a mild counter-rotating region in the envelope towards the surface of the star rotating at frequency  $-717 \pm 412$  nHz with the sign change occurring around  $r \sim 0.7 R_*$ . On the other hand, if we assume a discontinuous two-zone profile, we find an outer envelope rotating about six times slower than the overshoot region, at 49nHz. The averaging kernel associated with the outer zone of this two-zone model leads to a weighted average over most of the radiative envelope. The best counter-rotating profiles from inversion, when averaged over the radiative zone using this outer zone averaging kernel, lead to rotation rates entirely consistent between the two models.

We performed model comparisons based on the Akaike Information Criterion as well as the leave-one-out cross-validation technique, which are both better suited than the reduced  $\tilde{\chi}^2$  when comparing the performance of models that are not-nested, as is the case for the models we considered in this study. Both methods give preference to the inversion models with the presence of a mild counter-rotation in the radiative envelope at  $1\sigma$  level. The Monte Carlo simulations, fully independent of the above, are consistent with such result. Current stellar structure models have so far not considered this type of physical ingredient.

Following the first rough estimates of  $\Omega_{\text{core}}/\Omega_{\text{envelope}}$  for three core-hydrogen burning B stars prior to the asteroseismology space era (Aerts et al. 2003; Pamyatnykh et al. 2004; Briquet et al. 2007), the recent studies by Kurtz et al. (2014) and Saio et al. (2015) made the

first high-precision asteroseismic measurement of surface-to-core rotation in two  $\sim 1.5 M_{\odot}$  main-sequence hybrid heat-driven pulsators from four years of *Kepler* photometry. They found the star KIC 11145123 to have slightly faster envelope than core rotation and an average rotation period  $\sim 100$  d, while KIC 9244992 has slightly faster core than envelope rotation and an average rotation period of  $\sim 65$  d. The authors deduced these results from the measured rotationally split g-mode triplets and p-mode triplets and quintuplets without relying on forward seismic modeling of the zonal modes as we have done in the present work. Our study of the  $3.2 M_{\odot}$  main-sequence B-type star KIC 10526294 hints to an envelope whose inner rotation rate is opposite to its outer rate with a small factor ranging from  $\sim -0.06$  to  $\sim -0.2$  taking into account the uncertainties, while the star has a depth-averaged rotation period of about 186 d. In these three cases, even after taking into account that rotation rates at stellar birth have been largely overestimated (e.g., Zwintz et al. 2014), a strong and efficient mechanism must have been at work to slow down these stars’ rotation after their birth. Moreover, an efficient mechanism must be active to transport angular momentum within the star. Internal gravity waves (IGWs) could be viable as such a mechanism. Indeed, numerical simulations based on IGWs for a  $3 M_{\odot}$  star by Rogers et al. (2013) have shown that such waves can transfer angular momentum on short timescales and over the appropriate distances in stars with a convective core and a radiative envelope. Additionally, the study by Rogers et al. (2013) led to the conclusion that IGWs can lead to either a slightly faster envelope than core rotation, or an outer envelope rotating opposite to the inner regions. This mechanism thus could be the natural cause of the observational results on the rotational properties of KIC 10526294, KIC 11145123, and KIC 9244992.

The type of rotation profile found for KIC 10526294 and KIC 11145123 is not achieved in any standard stellar evolutionary scenario. A similar but much stronger discrepancy between models and observations occurs for the core rotation of red giants (e.g., Cantiello et al. 2014). In a next step, we do not only plan to perform similar studies as this one for OB-type stars with various stellar parameters, but we will also investigate how the stellar structure, and in particular the density profile, behaves during the evolution of the star in the presence of the most likely rotation profiles we found in this study, testing new physical ingredients such as internal gravity waves that were not yet included to describe the physics in the radiative envelope of massive stars. Only an extension of the sample of stars with seismic inversion treated with appropriate statistical model selection and coupled to an iterative procedure to upgrade the input physics can deliver a meaningful improvement in the stellar models. Our study is a first step in this direction for massive stars.

The authors thank Profs. Geert Molenberghs and Marc Aerts of the Center for Statistics, University of Hasselt, Belgium, for enlightening discussions and valuable advice on statistical

model selection. They also acknowledge detailed comments from a referee, which helped them to present the results in a more consistent way. Further, they are grateful to the *Kepler* team and everybody who has contributed to making this mission possible. Funding for the *Kepler* Mission was provided by NASA’s Science Mission Directorate. The research leading to these results has received funding from the Fund for Scientific Research of Flanders (FWO, grant number G.0728.11). E.M. is beneficiary of a postdoctoral grant from the Belgian Federal Science Policy Office (Belspo) co-funded by the Marie Curie Actions FP7-PEOPLE-COFUND2008 no. 246540 MOBILITY GRANT from the European Commission. Funding for the Stellar Astrophysics Centre is provided by The Danish National Research Foundation (Grant DNR106). The research is supported by the ASTERISK project (ASTERoseismic Investigations with SONG and Kepler) funded by the European Research Council (Grant agreement no. 267864).

A. Appendix A: Results for Error Set 2 and/or for limited triplet sets

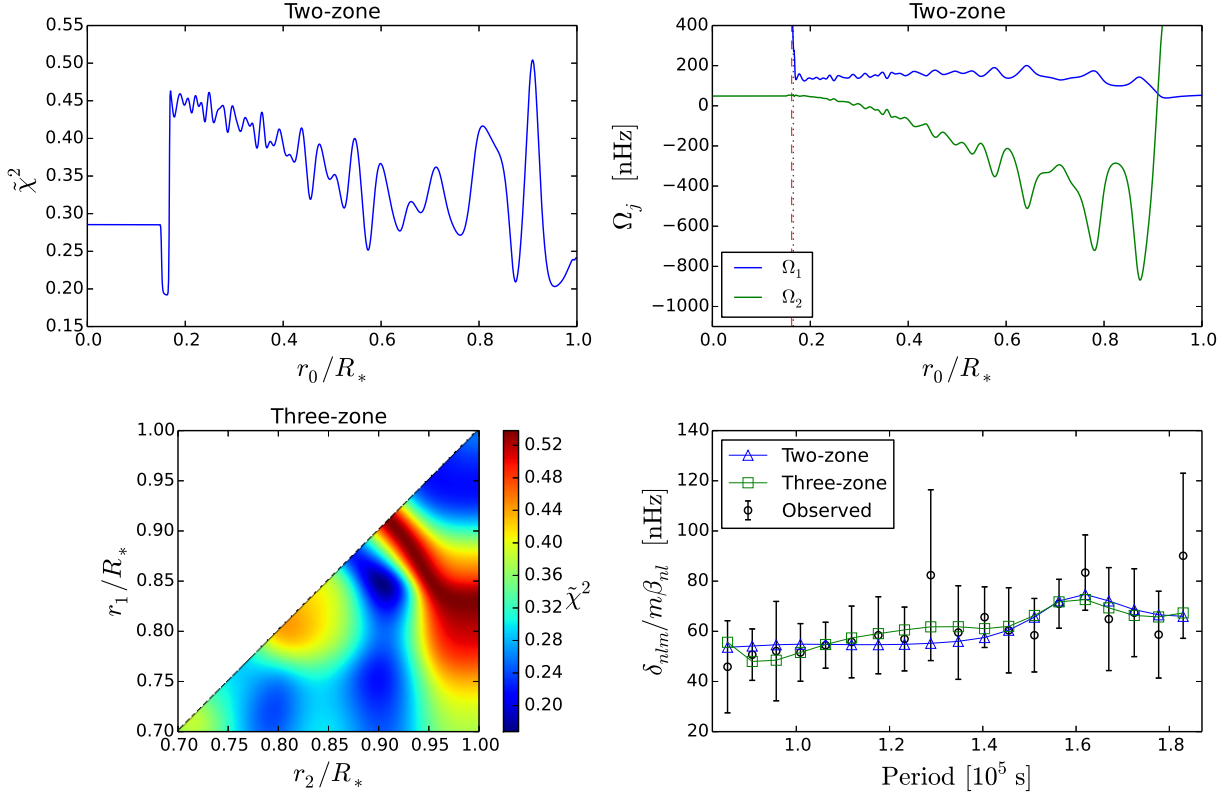


Fig. 19.— Same as Fig.8 with the exception that Error Set 2 has been used. The vertical dashed line in the top, right panel marks the location of the minimum of  $\tilde{\chi}^2$  for the two-zone model.

Table 4. Same as Table 3 but using the observation uncertainties from Error Set 2.

Rotation Profile	<i>rms</i> error [nHz]	$\nu$	$\tilde{\chi}^2$	AICc
Constant	11.85	18.00	0.45	12.82
Linear	11.78	17.00	0.36	13.67
Linear+	11.66	16.00	0.45	18.05
Two-zone	9.61	16.00	0.19	13.93
Three-zone	8.44	15.00	0.17	17.13
RLS, $N = 8$	9.17	15.93	0.17	13.83
RLS, $N = 14$	10.29	16.09	0.26	14.66
SOLA, $N = 8$	9.46	14.30	0.22	20.80
SOLA, $N = 14$	7.59	11.48	0.15	35.90

Table 5. Same as Table 3 but excluding the three most asymmetric splittings, i.e., those with periods near  $0.96 \times 10^5$ s,  $1.29 \times 10^5$ s, and  $1.83 \times 10^5$ s. The single  $m = +1$  mode with period near  $1.78 \times 10^5$ s was also excluded. Error Set 1 is used.

Rotation Profile	<i>rms</i> error [nHz]	$\nu$	$\tilde{\chi}^2$	AICc
Constant	9.07	14.00	25.07	355.9
Linear	7.22	13.00	8.55	119.4
Linear+	8.29	12.00	22.08	277.0
Two-zone	4.95	12.00	1.69	32.27
Three-zone	5.16	11.00	0.53	22.46
RLS, $N = 8$	4.84	11.29	0.63	22.33
RLS, $N = 14$	4.77	11.20	2.35	42.00
SOLA, $N = 8$	5.86	9.45	0.86	34.48
SOLA, $N = 14$	3.58	7.21	0.40	53.45

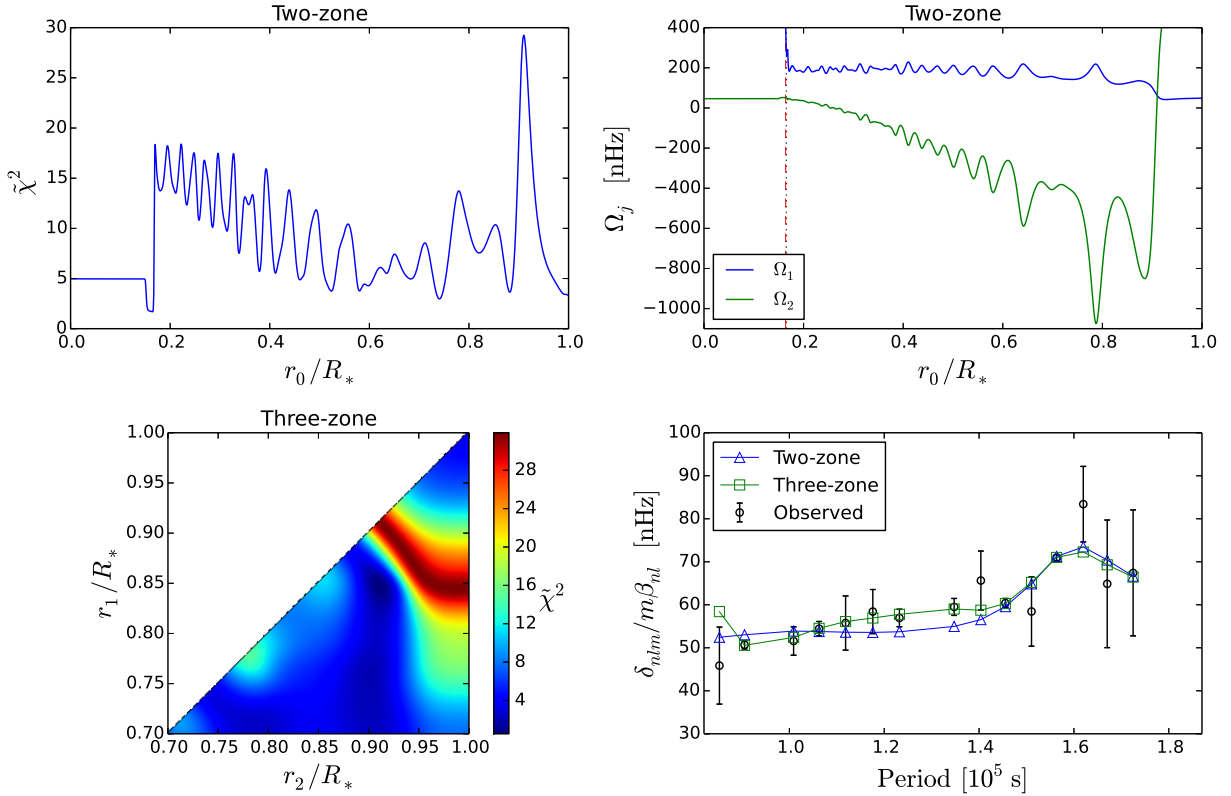


Fig. 20.— Same as Fig. 19 with the exception that the three most asymmetric splittings have been excluded from the  $\tilde{\chi}^2$  minimization, i.e. those with periods near  $0.96 \times 10^5$ s,  $1.29 \times 10^5$ s and  $1.83 \times 10^5$ s. The single  $m = +1$  splitting with period near  $1.78 \times 10^5$ s was also excluded. Error Set 1 has been used.

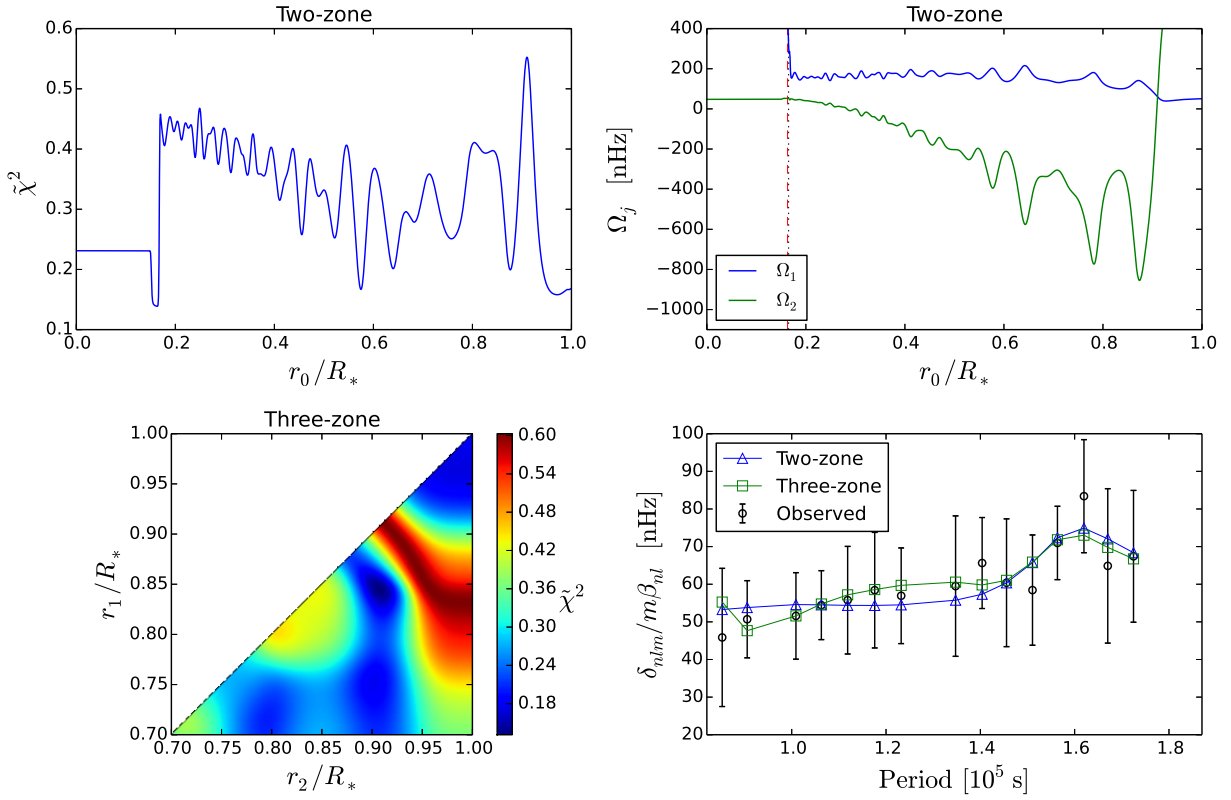


Fig. 21.— Same as Fig. 20, i.e., omitting the three most asymmetric modes and the single  $m = +1$  splitting, but this time using Error Set 2.

Table 6. Same as Table 5 but using the observation uncertainties from Error Set 2.

Rotation Profile	<i>rms</i> error [nHz]	$\nu$	$\tilde{\chi}^2$	AICc
Constant	8.95	14.00	0.47	11.63
Linear	7.05	13.00	0.32	12.36
Linear+	8.27	12.00	0.47	17.66
Two-zone	4.91	12.00	0.14	13.67
Three-zone	4.70	11.00	0.13	18.11
RLS, $N = 8$	4.96	12.15	0.14	13.11
RLS, $N = 14$	5.85	12.39	0.24	13.42
SOLA, $N = 8$	6.04	10.99	0.23	19.27
SOLA, $N = 14$	3.49	8.59	0.10	34.55

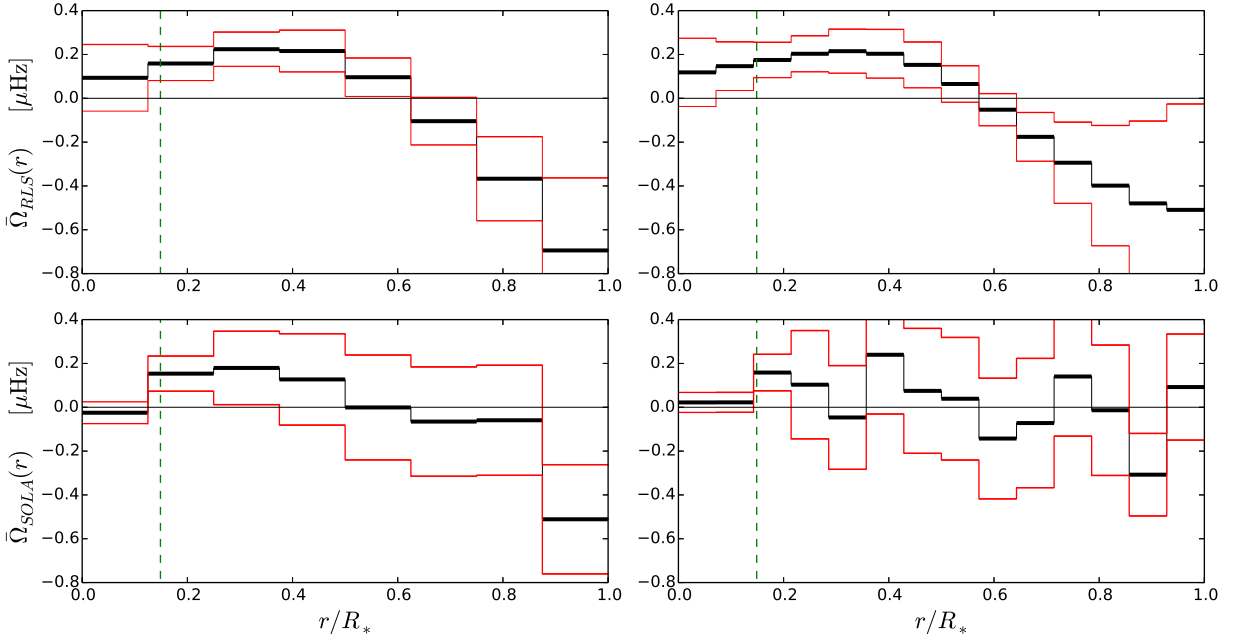


Fig. 22.— Same as Fig. 10 with the exception that Error Set 2 has been used.

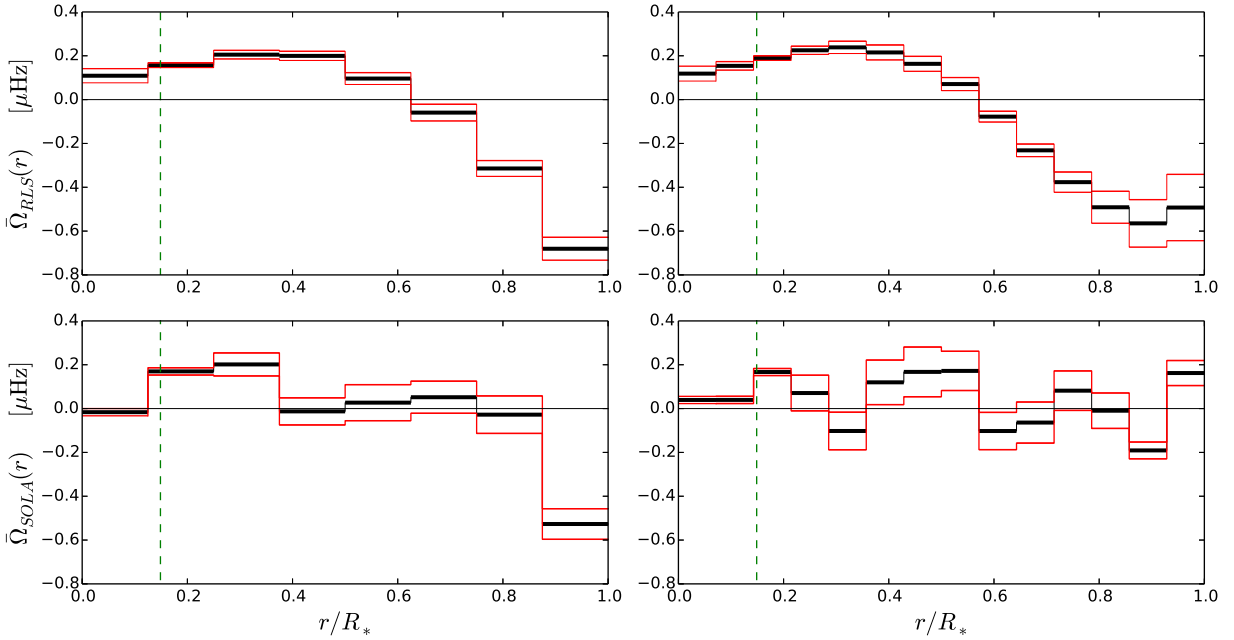


Fig. 23.— Same as Fig. 10 but this time excluding the three most asymmetric splittings, i.e., those with periods near  $0.96 \times 10^5$ s,  $1.29 \times 10^5$ s and  $1.83 \times 10^5$ s. The single  $m = +1$  mode with period near  $1.78 \times 10^5$ s was also excluded from the computation.



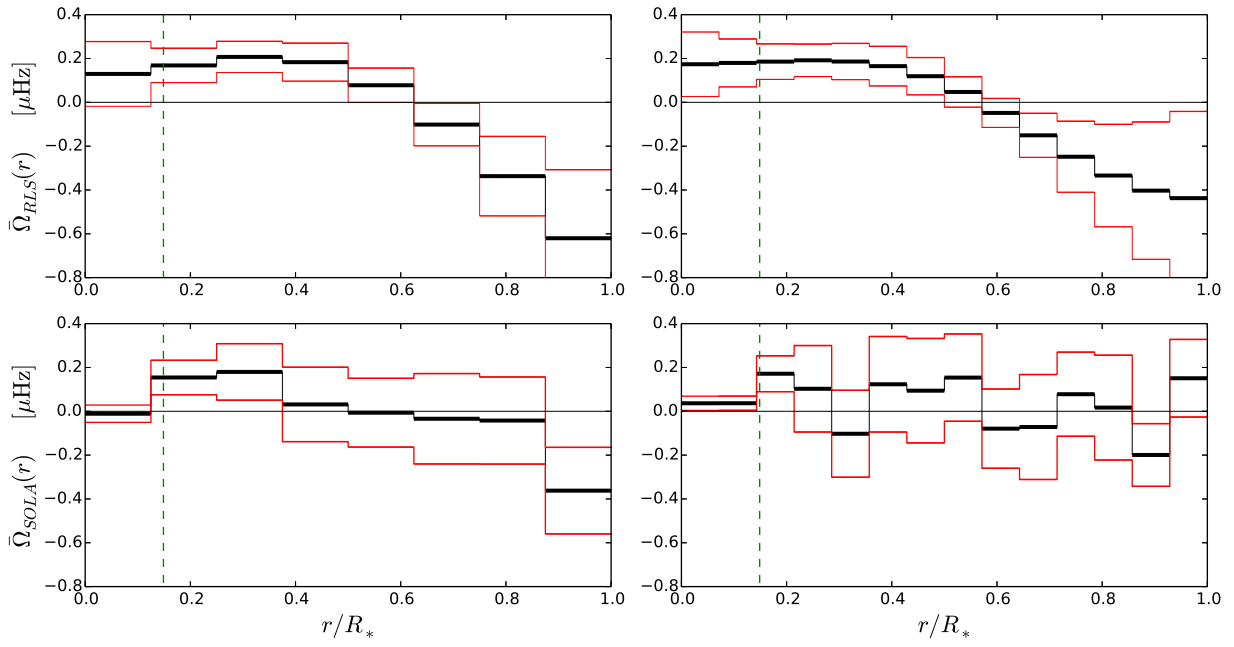


Fig. 24.— Same as Fig. 23 with the exception that Error Set 2 has been used.

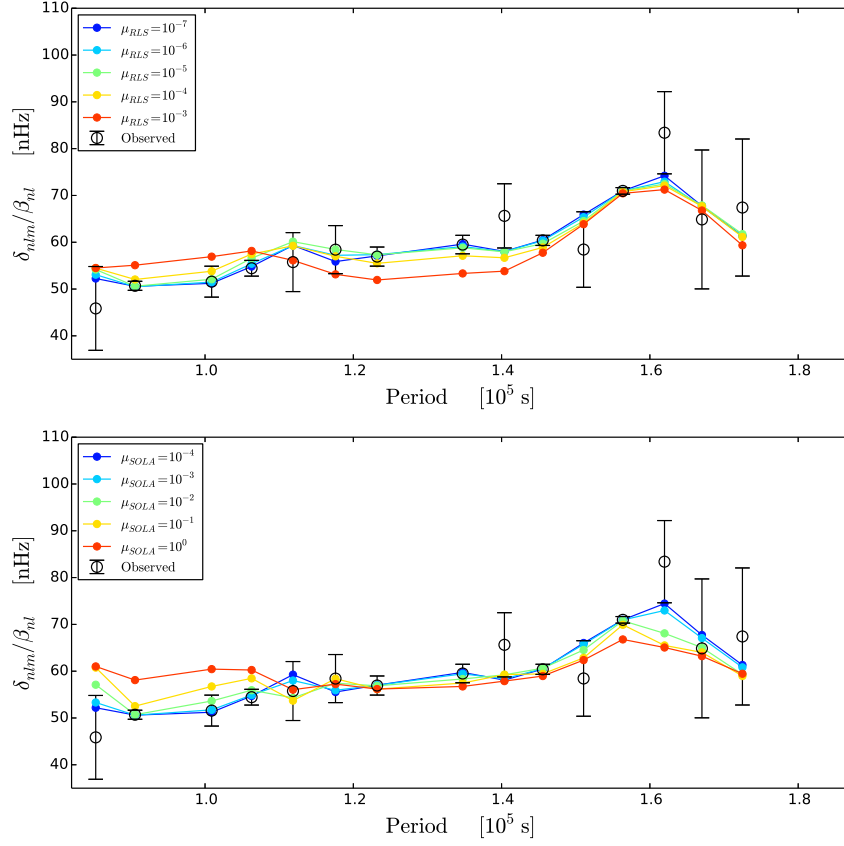


Fig. 25.— Same as Fig. 11 but excluding the three most asymmetric splittings, i.e., those with periods near  $0.96 \times 10^5$ s,  $1.29 \times 10^5$ s and  $1.83 \times 10^5$ s. The single  $m = +1$  mode with period near  $1.78 \times 10^5$ s was also excluded from the computation.

## B. Appendix B: The $\mathbf{A}$ matrices

As mentioned in Section 6, the matrix  $\mathbf{A}$  gives an indication of how well the inversion profile recovers the true profile (in the ideal case of no measurement error in the splittings). Using the best model from Moravveji et al. (2015), we can see this fact at work very clearly in both Figs. 26 and 27 as the respective  $\mu$  parameter is varied. The more  $\mathbf{A}$  resembles the identity matrix the better the reconstruction is, thus providing a qualitative assessment of the inversion.

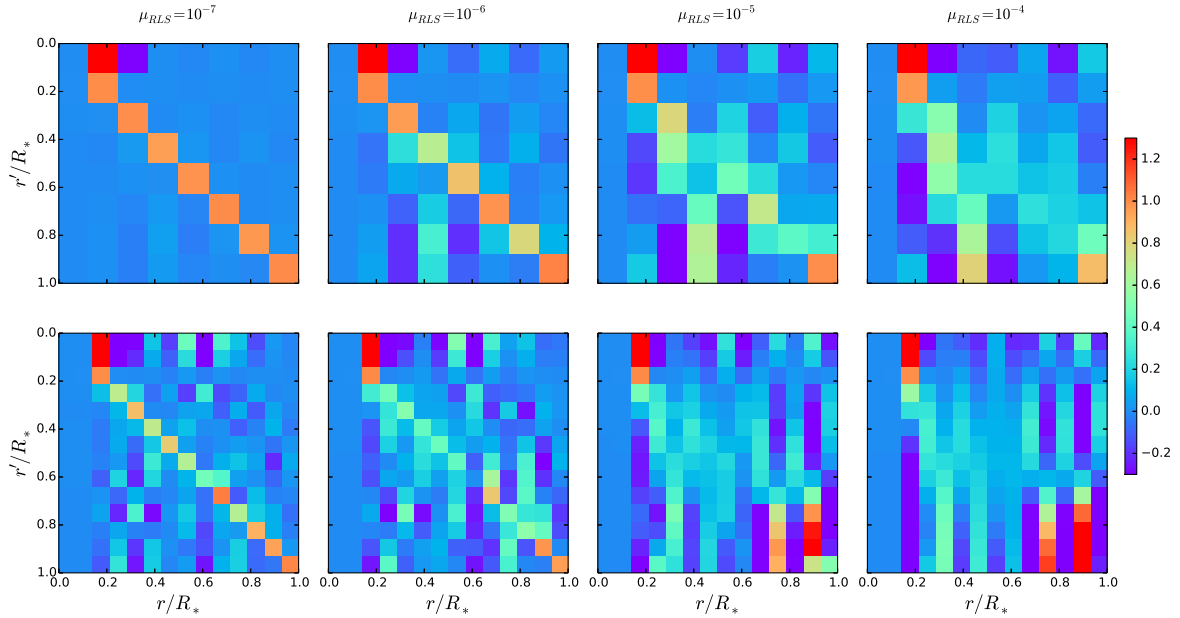


Fig. 26.— The matrix  $\mathbf{A}$  for the RLS method using the kernels from the best model in Moravveji et al. (2015) with two different resolutions ( $N = \{8, 14\}$ ; top and bottom row respectively) and a range of smoothing parameters  $\mu_{RLS}$ . Each row on these matrices is the discrete version of the averaging kernel  $\mathcal{K}(r', r)$ . The  $\mathbf{A}$  matrix should resemble as much as possible the identity matrix, as Eq. (13) indicates, if we want a faithful reconstruction of the rotation rate (at the radial location defined by the row index, i.e., first row corresponds to the first bin in the radial grid). Note how near  $r/R_* \sim 0.17$  the rotation rate is well recovered almost independently of the choice of  $N$  or  $\mu_{RLS}$ .

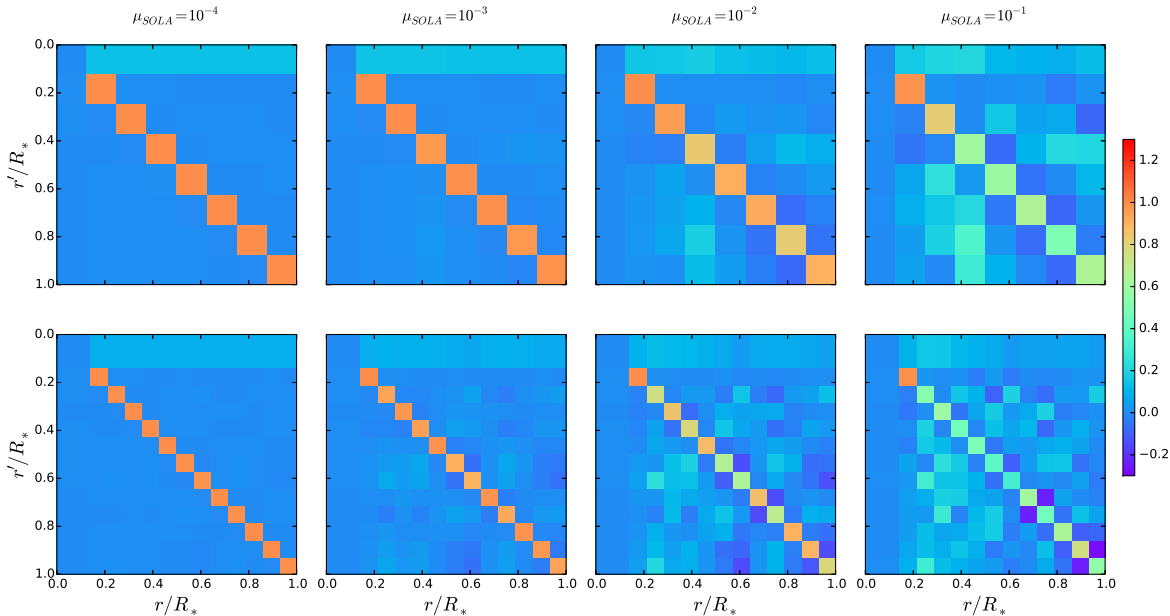


Fig. 27.— Same as in Fig. 26 but using the SOLA method. The matrices are very well localized except at higher resolutions and higher  $\mu_{SOLA}$ . At  $\mu_{SOLA} = 10^{-2}$  and  $N = 8$  there is a small amount of leakage from regions close to  $r = 0.4 R_*$  into the outer radial bins ( $r' \sim 0.9 R_*$ ). We estimate from this that the rotation rate there is overestimated by the inversion by about 3%.

### C. Appendix C: Averaging kernels in the continuous limit

The RLS and SOLA inversions behave very differently when the resolution is increased. In this section’s experiments we kept  $\mu_{RLS} = 10^{-5}$  and  $\mu_{SOLA} = 10^{-2}$  fixed but used three different resolutions,  $N = 14, 28, 5000$ . From the viewpoint of the inversion, it is possible to increase the resolution beyond the number of observations  $M$  since regularization keeps the *effective* number of fitted parameters below  $M$ . Here we do not include the variances on the inversions in the discussion. We have chosen the Error Set 1 as the uncertainties on the splittings.

In Fig. 28 we show the resulting inversion profiles. There are two radial locations where most of the rotation rates roughly coincide. One is at  $r \sim 0.17$  and the other one is at  $r \sim 0.92$  where the rotation values are not too far from each other except for the SOLA inversions with  $N = 28, 5000$ .

Let us examine the averaging kernels from three selected radial locations  $r_0 = 0.17 R_*$ ,

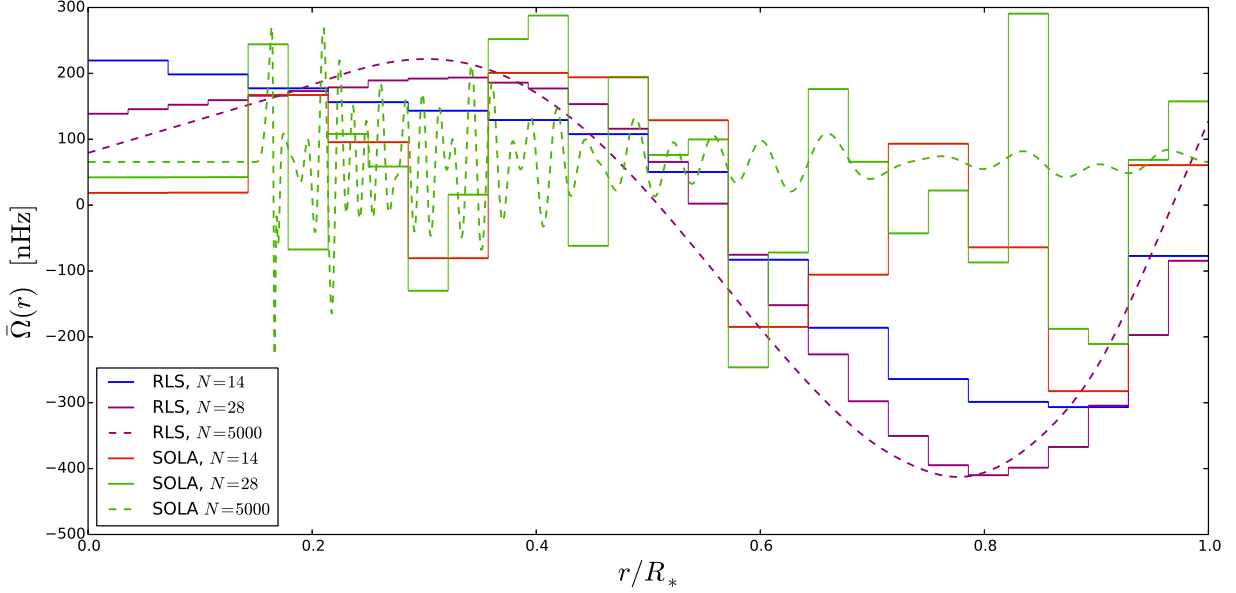


Fig. 28.— Rotation profiles from RLS ( $\mu_{RLS} = 10^{-5}$ ) and SOLA ( $\mu_{SOLA} = 10^{-2}$ ) methods and three different resolutions  $N = 14, 28, 5000$ . The inversions are based on the kernels from the best model of Moravveji et al. (2015). The measurement uncertainties are taken from the error set 2.

$r_0 = 0.48 R_*$  and  $r = 0.92 R_*$  as shown in Figures 29, 30 and 31, respectively. From the figures we see that for  $r_0 = 0.17 R_*$  all the averaging kernels are indeed well behaved generally, so we expect inferences for this location to be consistent. At  $r_0 = 0.48$  (Figure 30) the localization is acceptable as long as  $N$  is low. Closer to the stellar surface, at  $r_0 = 0.92$  (Fig. 31), the situation is similar although the RLS kernels degrade considerably already when  $N = 28$ .

From these figures we conclude that consistent inferences are to be found using either RLS or SOLA methods if the resolution is kept low, i.e.,  $N \lesssim 14$ . Such a resolution also implies a sensible model comparison through the AICc (see Table 3), while larger  $N$  and small smoothing parameters would lead to an effective number of degrees of freedom  $\nu < 1$  and strongly negative AICc values, implying overfitting from the viewpoint of model comparison.

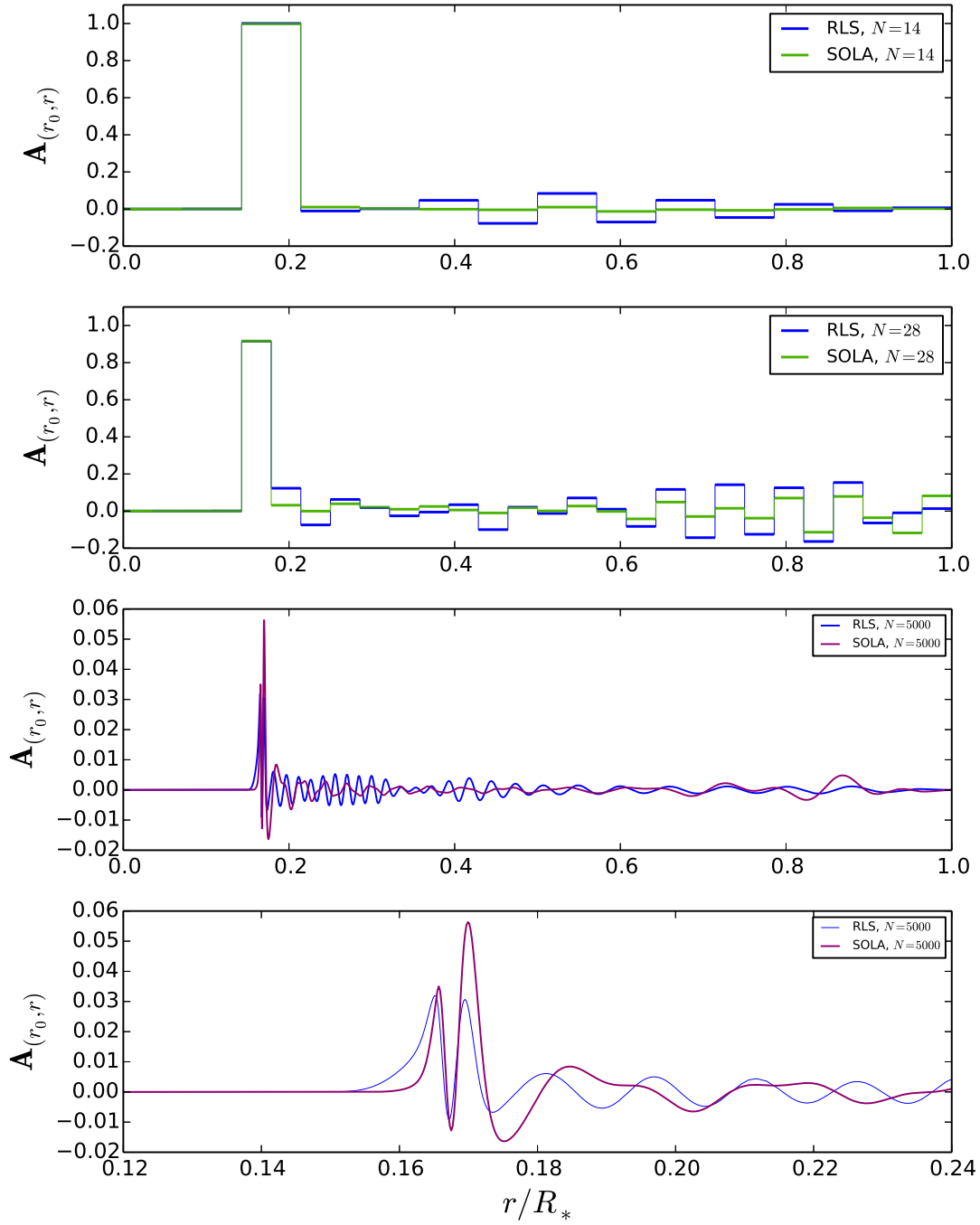


Fig. 29.— The row of  $\mathbf{A}$  corresponding to  $r_0 = 0.17$  at three resolutions (top three plots). Bottom plot is a zoom of the one immediately above.

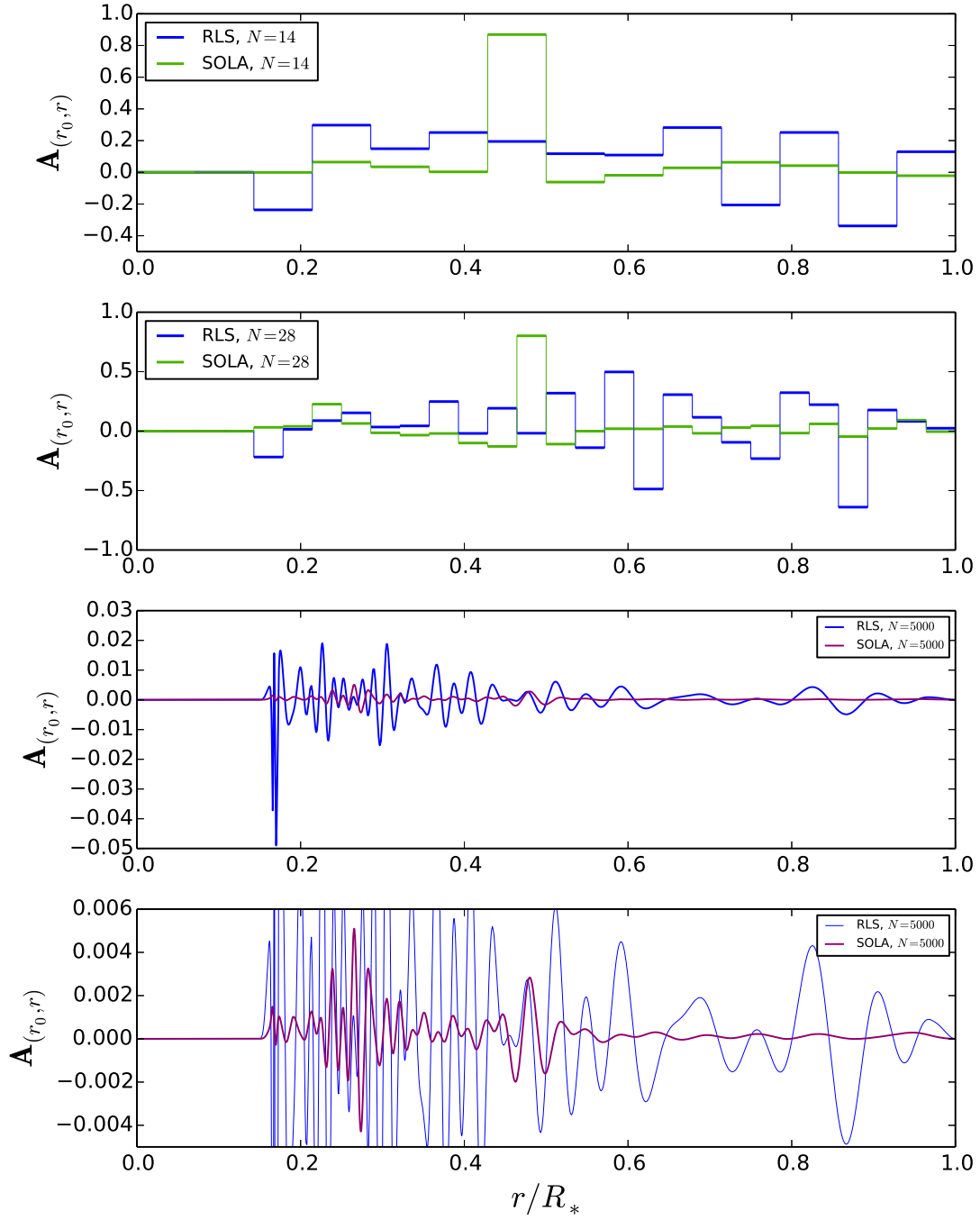


Fig. 30.— Same as Figure 29 but for  $r_0 = 0.48$ .

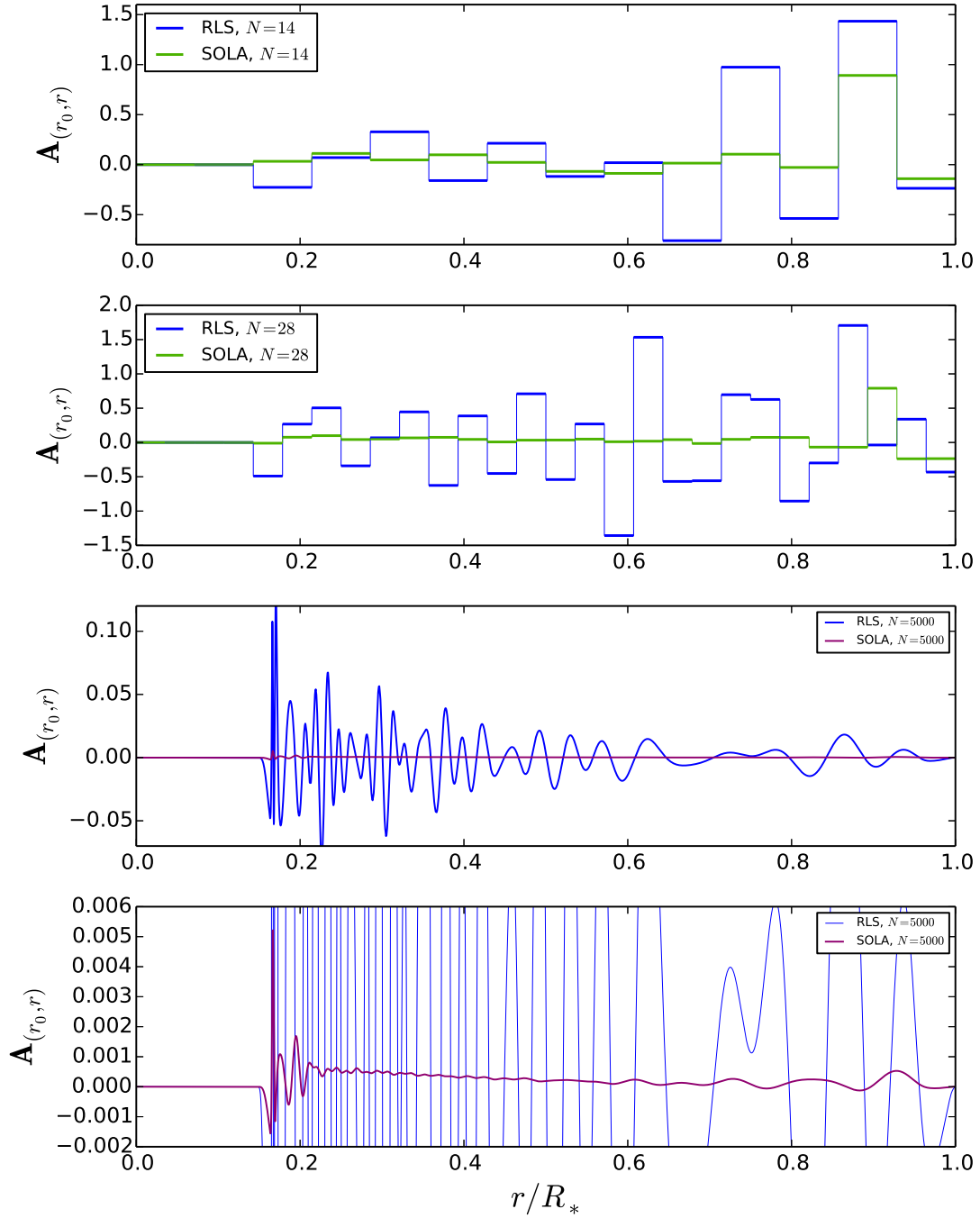


Fig. 31.— Same as Figure 30 but for  $r_0 = 0.92$ .



### D. Appendix D: Testing RLS inversions with a synthetic profile

The following test is to check that the counter-rotation profiles are not produced by some undesired property of the RLS inversion methods. We take the optimum two-zone model from Section 5 and smooth it using the ‘low pass’ filter with correlation length  $\lambda = 0.3$  described in Section 7. This is taken as the ‘actual’ rotational profile, which does not exhibit counter-rotation. Subsequently, we calculate the associated exact rotational splittings via Eq. (2). To each of these 19 splittings we add random noise sampled from a Gaussian distribution with zero mean and the same standard deviation as the actual measurement errors (Error Set 1). We set  $N = 8$ ,  $\mu_{\text{RLS}} = 10^{-5}$  as used for the RLS inversions in the main text and proceed to calculate the inversion profile.

At each radial bin we compare the inversion value with the integral average of the ‘actual’ profile over the same radial bin. This gives us a direct estimate of the inversion error. By repeating this process a large number of times we can obtain well defined statistics (we used  $10^7$  iterations). Figure 32 shows the ‘actual’ profile in blue, the recovered profile in black and the estimated  $1\sigma$  uncertainty range in red. The RLS method does a good job in recovering the actual profile, which always occurs within the errors. Some inversion profiles must counter-rotate mildly since the error region extends below zero in the outer half of the star. However, given the errors, we do not find a counter-rotating profile in this case.

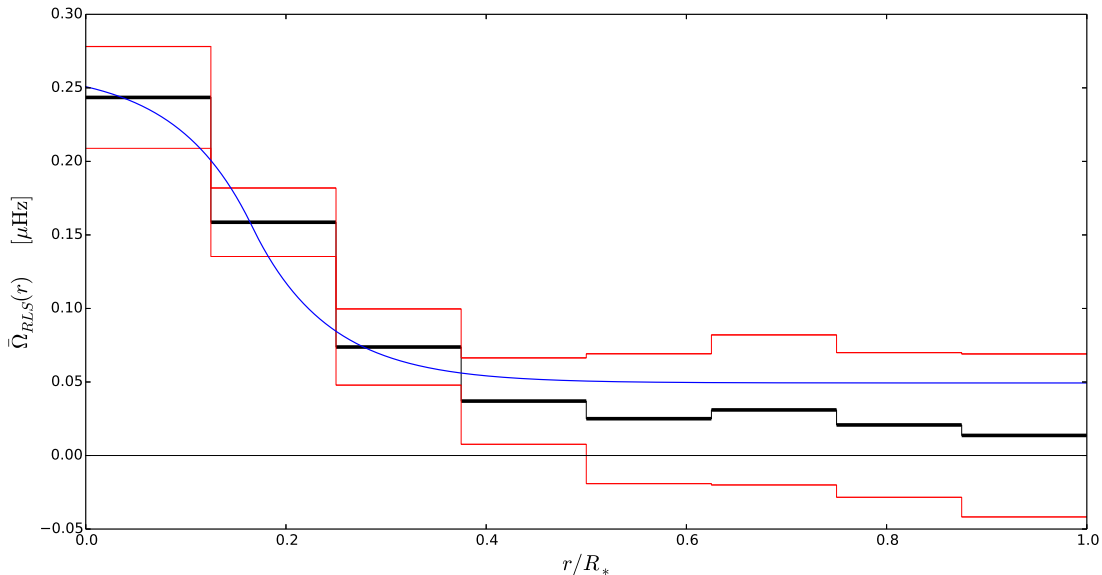


Fig. 32.— The smoothed-out two-zone model (blue, correlation length  $\lambda = 0.3$ ) and the recovered profile from RLS inversion (black,  $\mu_{\text{RLS}} = 10^{-5}$ ). Error bounds are in red.

## REFERENCES

- Aerts, C., Christensen-Dalsgaard, J., & Kurtz, D. W. 2010, *Asteroseismology*, Astronomy and Astrophysics Library (Springer Heidelberg)
- Aerts, C., Thoul, A., Daszyńska, J., et al. 2003, *Science*, 300, 1926
- Beck, P. G., Montalbán, J., Kallinger, T., et al. 2012, *Nature*, 481, 55
- Beck, P. G., Hambleton, K., Vos, J., et al. 2014, *A&A*, 564, A36
- Boyd, S., & Vandenberghe, L. 2004, *Convex Optimization* (Cambridge University Press)
- Briquet, M., Morel, T., Thoul, A., et al. 2007, *MNRAS*, 381, 1482
- Burnham, K., & Anderson, D. 2002, *Model Selection and Multimodel Inference: A Practical Information-Theoretic Approach* (Springer)
- Cantiello, M., Mankovich, C., Bildsten, L., Christensen-Dalsgaard, J., & Paxton, B. 2014, *ApJ*, 788, 93
- Charpinet, S., Fontaine, G., & Brassard, P. 2009, *Nature*, 461, 501
- Christensen-Dalsgaard, J. 2002, *Reviews of Modern Physics*, 74, 1073
- Córsico, A. H., Althaus, L. G., Kawaler, S. D., Miller Bertolami, M. M., & García-Berro, E. 2012, in *Astronomical Society of the Pacific Conference Series*, Vol. 462, *Progress in Solar/Stellar Physics with Helio- and Asteroseismology*, ed. H. Shibahashi, M. Takata, & A. E. Lynas-Gray, 176
- Craig, I., & Brown, J. 1986, *Inverse problems in astronomy: a guide to inversion strategies for remotely sensed data* (A. Hilger)
- Degroote, P., Briquet, M., Catala, C., et al. 2009, *A&A*, 506, 111
- Degroote, P., Aerts, C., Baglin, A., et al. 2010, *Nature*, 464, 259
- Deheuvels, S., García, R. A., Chaplin, W. J., et al. 2012, *ApJ*, 756, 19
- Deheuvels, S., Doan, G., Goupil, M. J., et al. 2014, *A&A*, 564, A27
- Eggenberger, P., Montalbán, J., & Miglio, A. 2012, *A&A*, 544, L4
- Gough, D. 1985, *Sol. Phys.*, 100, 65

- Hasan, S. S., Zahn, J.-P., & Christensen-Dalsgaard, J. 2005, *A&A*, 444, L29
- Hastie, T., Tibshirani, R., & Friedman, J. 2009, *The Elements of Statistical Learning: Data Mining, Inference, and Prediction*, Springer series in statistics (Springer)
- Hurvich, C. M., & Tsai, C.-L. 1989, *Biometrika*, 76, 297
- Kawaler, S. D., & Bradley, P. A. 1994, *ApJ*, 427, 415
- Kawaler, S. D., Sekii, T., & Gough, D. 1999, *ApJ*, 516, 349
- Kuhn, H. W., & Tucker, A. W. 1951, in *Proceedings of the Second Berkeley Symposium on Mathematical Statistics and Probability* (Berkeley, Calif.: University of California Press), 481–492
- Kurtz, D. W., Saio, H., Takata, M., et al. 2014, *MNRAS*, 444, 102
- Ledoux, P. 1951, *ApJ*, 114, 373
- Maeder, A. 2009, *Physics, Formation and Evolution of Rotating Stars*, Astronomy and Astrophysics Library (Springer Heidelberg)
- Moravveji, E., Aerts, C., Pápics, P. I., Andres Triana, S., & Vandoren, B. 2015, *A&A*, in press (arXiv:1505.06902)
- Mosser, B., Goupil, M. J., Belkacem, K., et al. 2012, *A&A*, 548, A10
- Pamyatnykh, A. A., Handler, G., & Dziembowski, W. A. 2004, *MNRAS*, 350, 1022
- Pápics, P. I., Moravveji, E., Aerts, C., et al. 2014, *A&A*, 570, A8
- Paxton, B., Bildsten, L., Dotter, A., et al. 2011, *ApJS*, 192, 3
- Paxton, B., Cantiello, M., Arras, P., et al. 2013, *ApJS*, 208, 4
- Pijpers, F. P., & Thompson, M. J. 1994, *A&A*, 281, 231
- Rogers, T. M., Lin, D. N. C., McElwaine, J. N., & Lau, H. H. B. 2013, *ApJ*, 772, 21
- Saio, H., Kurtz, D. W., Takata, M., et al. 2015, *MNRAS*, 447, 3264
- Thompson, M. J., Christensen-Dalsgaard, J., Miesch, M. S., & Toomre, J. 2003, *ARA&A*, 41, 599
- Townsend, R. H. D., & Teitler, S. A. 2013, *MNRAS*, 435, 3406

Triana, S. A., Zimmerman, D. S., Nataf, H.-C., et al. 2014, *New Journal of Physics*, 16, 113005 (arXiv:1410.3641)

van Saders, J. L., & Pinsonneault, M. H. 2013, *ApJ*, 776, 67

Zwintz, K., Fossati, L., Ryabchikova, T., et al. 2014, *Science*, 345, 550